

A SURVEY OF GALAXY KINEMATICS TO $z \sim 1$ IN THE TKRS/GOODS-N FIELD. I. ROTATION AND DISPERSION PROPERTIES¹

BENJAMIN J. WEINER², CHRISTOPHER N.A. WILLMER^{3,4}, S.M. FABER⁵, JASON MELBOURNE⁵, SUSAN A. KASSIN⁵, ANDREW C. PHILLIPS⁵, JUSTIN HARKER⁵, A.J. METEVIER^{6,7}, N.P. VOGT⁸, D.C. KOO⁵

Accepted by ApJ

ABSTRACT

We present kinematic measurements of a large sample of galaxies from the Team Keck Redshift Survey in the GOODS-N field. We measure line-of-sight velocity dispersions from linewidths of integrated emission for 1089 galaxies with median redshift 0.637, and spatially resolved kinematics for a subsample of 380 galaxies. This is the largest sample of galaxies to $z \sim 1$ with kinematics to date, and allows us to measure kinematic properties without morphological pre-selection. Emission linewidths provide a dynamical measurement for the bulk of the blue galaxy population. To fit the spatially resolved kinematics, we construct models with both line-of-sight rotation amplitude and velocity dispersion as fit parameters. Integrated linewidth correlates well with a combination of the spatially-resolved velocity gradient and dispersion, and is a robust measure of galaxy kinematics. The spatial extents of emission and continuum are similar and there is no evidence that linewidths are affected by nuclear or clumpy emission. The measured rotation gradient is a strong function of slit position angle alignment with galaxy major axis, but integrated linewidth is largely independent of slit alignment. Even in a subsample of galaxies with well-aligned slits, there are galaxies whose kinematics are dominated by dispersion ($V/\sigma < 1$) rather than rotation. These are probably objects with disordered velocity fields, not dynamically hot stellar systems. About 35% of the spatially resolved sample are dispersion dominated; galaxies that are both dispersion dominated and bright exist at high redshift but appear rare at low redshift. This kinematic morphology may yield a probe of the evolutionary state of these objects. Kinematic morphology is linked to photometric morphology in HST/ACS images: dispersion dominated galaxies include a higher fraction of irregulars and chain galaxies, while rotation dominated galaxies are mostly disks and irregulars. Only one-third of chain/hyphen galaxies are dominated by rotation; high redshift elongated objects cannot be assumed to be inclined disks. In a companion paper, we use the linewidths and rotation to measure evolution in the Tully-Fisher relation.

Subject headings: galaxies: distances and redshifts — galaxies: evolution — galaxies: fundamental parameters — galaxies: high-redshift — galaxies: structure — surveys

1. INTRODUCTION

Galaxy redshift surveys to $z \sim 1$ allow the measurement of evolution in properties of the galaxy population at lookback times of half the present age of the Universe. To date, a number of surveys have studied galaxy properties such as luminosities, colors, radii, morphology and environment. The internal kinematics of galaxies are equally interesting, as a physical probe of individual objects and to allow the measurement of scaling relations of the galaxy population. However, measuring kinematics requires moderate to high-resolution spectroscopy, which has until recently been difficult to obtain for large num-

bers of faint galaxies.

This paper measures kinematics of galaxies from emission lines, using Keck/DEIMOS spectra from the Team Keck Redshift Survey (TKRS) in the GOODS-N (Great Observatories Origins Deep Survey) field (Wirth et al. 2004; Giavalisco et al. 2004). The TKRS provides spectra of 1437 galaxies drawn from a magnitude limited sample to $R_{AB} < 24.4$, at resolution $R \sim 2100$. We select 1191 galaxies with good emission line detections and measure 1089 emission line velocity dispersions from integrated emission, with median $\langle z \rangle = 0.637$. A subsample of 464 are selected for modeling spatially resolved rotation and dispersion profiles, of which 380 yield good-quality measurements. We use these spatially resolved measures to probe the kinematic properties of high redshift galaxies and to test the integrated linewidths. In Paper II (Weiner et al. 2006), we use the linewidths and rotation velocities to measure evolution in the Tully-Fisher relation.

A number of previous works have observed galaxy internal kinematics from $0.1 < z < 1.0$, for the purpose of measuring Tully-Fisher relations. The pioneering studies of Vogt et al. (1996, 1997) modeled rotation curves for 17 galaxies of disky morphology with median $\langle z \rangle = 0.47$ by combining Keck/LRIS slitlet spectra with structural information from HST photometry. Several subsequent studies of rotation curves with similar modeling proce-

¹ Based in part on observations taken at the W.M. Keck Observatory, which is operated jointly by the University of California and the California Institute of Technology

² Department of Astronomy, University of Maryland, College Park, MD 20742, bjw@astro.umd.edu Present address: Steward Observatory, University of Arizona, 933 N. Cherry Av., Tucson, AZ 85721

³ Steward Observatory, University of Arizona, 933 N. Cherry Av., Tucson, AZ 85721

⁴ On leave from Observatorio Nacional, Rio de Janeiro, Brasil

⁵ UCO/Lick Observatory, University of California, Santa Cruz, Santa Cruz, CA 95064

⁶ Center for Adaptive Optics, University of California, Santa Cruz, Santa Cruz, CA 95064

⁷ NSF Astronomy and Astrophysics Postdoctoral Fellow

⁸ Department of Astronomy, New Mexico State University, P. O. Box 30001, Las Cruces, NM 88003

dures have contained 20-100 galaxies with median redshifts $\sim 0.4 - 0.5$ (e.g. Simard & Pritchett 1998; Vogt 2000; Ziegler et al. 2002; Milvang-Jensen et al. 2003; Böhm et al. 2004; Bamford et al. 2005, 2006; Conselice et al. 2005; Nakamura et al. 2006; Metevier et al. 2006). Generally these samples have been morphologically selected to be inclined disk objects, of which a majority show measurable rotation.

Here we study a sample with emission line kinematics that is essentially selected only on magnitude and emission line strength. We measure one-dimensional integrated velocity dispersion (linewidth), and for a subsample, spatially resolved rotation profiles; we discuss the properties of these velocity measures in Sections 4 and 5. We show that the integrated linewidth is a fairly robust measure of the characteristic velocity of a galaxy, expanding the scope of the study beyond galaxies that are selected to be orderly rotating disks. Indeed, we find from the spatially resolved rotation profiles that a significant number of high-redshift galaxies show kinematics that do not appear to be orderly rotation.

We adopt a Λ CDM cosmology with $h = 0.7$, $\Omega_M = 0.3$, and $\Omega_\Lambda = 0.7$. Magnitudes quoted in this paper are in the AB system unless explicitly indicated as Vega. Section 2 discusses the sample and measurement methods, and section 3 presents the properties of the sample and completeness. Sections 4 and 5 study the simulated and empirical properties of the kinematic measurements: integrated linewidths and spatially resolved velocities. In Paper II we use the kinematics to measure the evolution in the Tully-Fisher relation with redshift.

2. SAMPLE, VELOCITY MEASUREMENTS, AND PHOTOMETRY

2.1. Properties of the spectroscopic sample

The parent sample for our kinematic measurements is the Team Keck Redshift Survey (TKRS) in the GOODS-N field. The selection and observations are described at length by Wirth et al. (2004) and we present a few relevant details here. Data and images of TKRS galaxies may be retrieved from the TKRS website at <http://www2.keck.hawaii.edu/science/tksurvey/>.

The TKRS sample is magnitude selected to $R_{AB} = 24.4$. No color or morphological selection was applied, but there is a mild surface brightness selection (see Willmer et al. 2006), which may eliminate a few faint high- z reddened edge-on galaxies. The sampling completeness (ratio of galaxies with spectra to galaxies meeting selection criteria) is $\sim 75\%$ and the redshift success rate is $\sim 70\%$ ($> 80\%$ for $R_{AB} < 23$). Most galaxies for which spectra were taken but redshifts could not be determined are faint, blue, and probably at $z > 1.5$, where $[\text{O II}] \lambda 3727$ disappears into the night-sky OH line forest.

TKRS observations used the Keck II telescope and DEIMOS spectrograph with a 600 lines/mm grating, yielding a sampling of $0.119''/\text{pixel}$ and $0.648 \text{ \AA}/\text{pixel}$. Typical wavelength coverage was 4600–9800 \AA . 18 slit-masks were observed, each for 60 minutes total exposure time. The slit width was $1.0''$. In the mask designs, slit position angles (PAs) could be tilted to follow the major axis of elongated objects, by up to 30 degrees away from the nominal perpendicular-to-dispersion direction. Galaxy PAs were measured from ground-based R -band imaging before mask design. When slits were tilted, the

slit width was adjusted to keep the width along the dispersion direction at $1.0''$, keeping the spectral resolution constant regardless of slit PA.

The TKRS data were reduced and redshifts measured with the DEIMOS pipeline software developed by the DEEP project, described in Davis et al. (2003) and Wirth et al. (2004); TKRS data are very similar to DEEP2 data, save that DEEP2 uses a 1200 lines/mm grating. Candidate redshifts were measured automatically and verified by visual inspection by members of Team Keck.

End data products include 2-d spectra for each slitlet and both optimal and boxcar extracted 1-d spectra for each object. We used the 2-d spectra to measure rotation curves and the 1-d spectra to measure linewidths of integrated emission. In this paper we always use the boxcar extraction, never the optimal: the optimal extraction weights different regions of the galaxy light profile unequally, which makes the physical meaning of the optimally extracted spectrum somewhat obscure. The boxcar extraction window diameter is set by the reduction software to 1.5 times the FWHM of the object measured in the 2-d spectrum. For nearly all galaxies, larger extraction windows do not make a significant difference to the measured linewidths, because the emission intensity is centrally peaked (see also Section 4.2).

2.2. Emission line measurement in the 1-d spectra

Our goal in fitting linewidths to integrated emission is to obtain a kinematic measurement for as many galaxies as possible, without applying cuts to the sample. Several previous studies have used linewidths of integrated emission to measure kinematics of small samples of galaxies at intermediate redshift (Rix et al. 1997; Mallen-Ornelas et al. 1999).

2.2.1. Line fitting

We developed an automated program to fit emission lines in all TKRS galaxies with secure redshifts (quality code 3 or 4 indicating two spectral features, Wirth et al. 2004). The LINEFIT program takes a galaxy redshift and list of common emission lines; at the predicted location of each line, it takes the wavelength, flux, and error data from a 40 \AA window and fits a gaussian profile, using a Levenberg-Marquardt non-linear least squares χ^2 minimization (Press et al. 1992).

The fit has four free parameters: continuum level, line intensity, velocity, and velocity dispersion. For the $[\text{O II}] \lambda\lambda 3726.0, 3728.8$ doublet, the program can fit a doublet with the wavelength ratio fixed and the intensity ratio fixed or free; for the TKRS data, we fixed the doublet intensity ratio at 1.4 (the mean ratio of red/blue components in high-S/N data measured with the 1200 lines/mm grating). The least squares fitter yields best-fit values and error estimates for all parameters. Fitting in the 40 \AA window does not provide an adequate measure of the continuum in low-S/N spectra and so LINEFIT also measures a robust continuum by taking the biweight of data in two 80 \AA windows on either side of the emission line.

2.2.2. Instrumental resolution

This sample relies heavily on the measurement of velocity dispersion, which in turn can be strongly affected

TABLE 1
DISPERSION AND VELOCITY-RELATED QUANTITIES

Quantity	units	description
σ_{obs}	\AA	Line dispersion measured in 1-d spectrum
σ_{inst}	\AA	Instrumental resolution
σ_{1d}	km s^{-1}	Intrinsic, instrumental-subtracted line-of-sight restframe dispersion in 1-d spectrum
V_{rot}	km s^{-1}	Restframe line-of-sight rotation velocity from modeling of 2-d spectrum
$V_{rot}/\sin i$	km s^{-1}	Inclination-corrected rotation velocity
σ_{2d}	km s^{-1}	Restframe line-of-sight intrinsic dispersion from modeling of 2-d spectrum
S_K	km s^{-1}	Combined velocity, $\sqrt{KV_{rot}^2 + \sigma_{2d}^2}$
V_c	km s^{-1}	True circular rotation velocity

by the instrumental spectral resolution σ_{inst} . Conventionally, the restframe intrinsic line-of-sight velocity dispersion σ_{1d} of a line is given by

$$\sigma_{1d} = \frac{c}{\lambda_{obs}} \sqrt{\sigma_{obs}^2 - \sigma_{inst}^2}, \quad (1)$$

where σ_{1d} is in km s^{-1} , λ_{obs} is the observed wavelength in \AA , and σ_{obs} and σ_{inst} are the measured line dispersion and instrumental resolution, both in \AA . As a rule of thumb, measurements for $\sigma_{1d} < c\sigma_{inst}/\lambda_{obs}$ are not very reliable because small errors in the observed width have a large effect on the inferred dispersion. We use σ_{1d} to denote the restframe velocity dispersion derived from the 1-dimensional extracted spectrum, which is integrated over the extraction window. Throughout these papers, observed quantities are given in \AA and restframe velocity quantities in km s^{-1} . This paper refers to several dispersion and velocity quantities, in observed and restframe, and 1-d and 2-d spectra; these are summarized in Table 1.

With DEIMOS and $1.0''$ slits, the profile of night sky lines or calibration arcs is somewhat flat-topped, less peaked than a gaussian. This flat-topping is pronounced for night sky lines in the 600 lines/mm grating data of the TKRS, but is relatively small for DEIMOS spectra taken with the 1200 lines/mm grating, such as those in the DEEP2 survey (Davis et al. 2003). Fitting gaussians to many line profiles of isolated night-sky lines in many different slits and masks yields mean instrumental gaussian sigmas $\sigma_{inst,sky} = 1.4, 0.56 \text{ \AA}$ for TKRS and DEEP2 respectively.

Flat-topping is less noticeable in the actual emission lines of observed galaxies in TKRS, for two reasons. First, galaxies' velocity widths broaden the profile so that flat-topping is smeared out. Second, TKRS galaxies are relatively small and their light distributions peak near the slit center, rather than uniformly filling the slit as night sky lines do. This slit underfilling is potentially a significant problem for any study of velocity dispersions of small objects. However, seeing and the relatively slow change of angular diameter with redshift beyond $z \sim 0.5$ mitigate the effect. The effect is also smaller when the instrumental resolution is moderately high, as in TKRS and even more so for DEEP2.

Modeling slit underfilling for the measured galaxy sizes

and comparing objects with both 600 and 1200 lines/mm observations shows that flat-topping and its opposing effects nearly cancel out. We matched observed linewidths for 70 galaxies on a DEEP2 slitmask that was observed with both 600 and 1200 lines/mm gratings, and found good agreement for 600 lines/mm $\sigma_{inst} = 1.4 \text{ \AA}$.

The instrumental resolution as measured from night sky lines varies by $\sim 5\%$ peak-peak over the DEIMOS field: lines from slitlets near the ends of the mask are broader than lines from slitlets near the center. The effect is only visible statistically, since its size is comparable to the scatter in individual sky line measurements and the scatter between different masks (focus variations). We have adopted a single value for the instrumental resolution and neglected spatial and temporal variations. The variations' effect on the derived dispersions is small: for a small galaxy with $\sigma_{1d} = 50 \text{ km s}^{-1}$, the peak error induced is $\sim 2 \text{ km s}^{-1}$, and the error declines rapidly for larger σ_{1d} .

2.2.3. Velocity dispersion sample

There are 1437 galaxies with redshifts, TKRS spectra, and magnitudes. We fit emission lines in each of these objects. For velocity dispersion purposes we then reject all lines that do not have a 4 sigma intensity detection. The 4 sigma line catalog contains 2595 lines over 1191 galaxies.

Galaxies can have several lines, and the fit parameters are independent. To obtain one estimate of velocity dispersion for each object, we take the weighted mean of the measurements of squared intrinsic velocity dispersion, σ_{1d}^2 ; using the square properly accounts for lines that are narrower than the nominal instrumental resolution, which have $\sigma_{1d}^2 < 0$. We use a weighted rms of the dispersions as the error estimate. We exclude a tail of 85 galaxies that have both $\text{error}(\log \sigma_{1d}) > 0.25$ and $\text{error}(\sigma_{1d}) > 30 \text{ km s}^{-1}$ to reject low-quality fits.

Some line fits have an observed width σ_{obs} that is smaller than the nominal instrumental width. Although this is formally physically impossible, it is expected in the presence of noisy data, slit underfilling, and variations in the instrumental resolution. After combining all lines, 196 of 1089 galaxies are “kinematically unresolved,” with widths close to or less than instrumental, so that the formal velocity dispersion is undefined or has a large error in $\log \sigma_{1d}$. When we restrict to $M_B < -18$, the cutoff for our Tully-Fisher fits in Paper II, 104 of 913 are kinematically unresolved in $\log \sigma_{1d}$, under the criteria $\text{error}(\log \sigma_{1d}) > 0.25$, $\text{error}(\sigma_{1d}) < 30$, and $\sigma_{1d} < 25 \text{ km s}^{-1}$. Eliminating these galaxies from the sample preferentially rejects low-velocity galaxies and leads to a bias, so for plotting and fitting purposes we assign them a low value, $\log \sigma_{1d} = 1.4 \pm 0.2$. The results of fitting do not depend strongly on the exact value assigned. Note that a few other galaxies have $\log \sigma_{1d} < 1.4$ yet low formal error on $\log \sigma_{1d}$, usually because they have very strong and well-measured emission lines. In Section 3 of Paper II we outline a fitting method which treats the unresolved galaxies more robustly by fitting the ensemble of observed width σ_{obs} before the instrumental resolution is subtracted.

Some galaxies with very bright emission lines can have formally very small errors. It is hubris to take these errors literally, since we can hardly expect to measure

velocity dispersions of distant galaxies to $< 5\%$. To be realistic and to prevent small errors from dominating fits, we add 0.03 in quadrature to the error on $\log \sigma_{1d}$, to cut off the low tail of the error distribution. The results are not sensitive to the exact value used; the median error for the sample of 913 brighter than $M_B = -18$ is 0.084 in $\log \sigma_{1d}$. As discussed in Paper II, the intrinsic scatter in $\log \sigma_{1d}$ dominates over the errors on individual points.

2.3. Rotation curve measurements

The DEIMOS slitlet spectra preserve spatial information and it is common to see emission lines with a velocity gradient. Spatially extended emission can be used to measure a rotation curve. However, the spatial extent of emission is only a few times the seeing, so “beam smearing” is large and the effect of seeing must be modeled. The rotation curve is also affected by the inclination, slit width, and slit alignment with respect to the major axis of the galaxy. We measured rotation curves for a subsample of objects in order to study the relation between rotation velocity and integrated linewidth.

2.3.1. Previous high-redshift rotation curve modeling

Previous efforts to measure rotation curves at intermediate to high redshifts have approached these problems by modeling the intrinsic emission intensity and velocity distribution, subjecting them to seeing and slit effects, and fitting models to the data to obtain a measure of the rotation velocity. Vogt et al. (1996, 1997) pioneered work in this field, using HST/WFPC2 imaging to model the galaxy light distribution and parameters such as inclination and position angle, and fitting to Keck/LRIS slit spectra, varying the model rotation velocity. Subsequent works in this field have followed similar modeling programs, applying seeing and slit effects to a 2-d model of the light and velocity fields (e.g. Simard & Pritchett 1998; Ziegler et al. 2002; Milvang-Jensen et al. 2003; Böhm et al. 2004; Bamford et al. 2005, 2006; Conselice et al. 2005; Nakamura et al. 2006; Metevier et al. 2006).

These programs have generally focused on relatively small numbers of galaxies ($\sim 10 - 100$), in some cases selected on morphology or spectra to be fairly normal rotating disks. They also require high-resolution imaging, preferably from HST, to obtain structural parameters. Most galaxies in the TKRS have deep HST/ACS imaging from the GOODS survey (Giavalisco et al. 2004), and full modeling of the rotation curves is in progress. However, such modeling requires fitting of structural parameters to ACS multidrizzled data and is beyond the scope of this paper.

2.3.2. Rotation curve modeling from spectra alone

In the spirit of obtaining kinematic measurements for as many galaxies as possible, we developed a simplified method for fitting seeing-compensated rotation curves using only the information contained in the 2-d spectra. This program, ROTCURVE, works by constructing models of the unblurred spatially resolved emission intensity, velocity and dispersion, blurring them along the slit to model seeing, and fitting to the data. Because it only has one dimension of spatial information, the rotation model and the seeing convolution are 1-d functions along the slit, and there is no compensation for disk inclination or slit position angle.

We chose a subsample of galaxies for rotation curve fitting using cuts in intensity of the strongest emission line and in spatial extent along the slit. The strongest emission line was required to have integrated intensity $> 3000 e^-/\text{pixel } \text{\AA}$ in the summed 1-d spectrum. A gaussian was fit to the light profile along the slit and we required $\sigma_{\text{light}} > 0.4''$, equivalent to $\text{FWHM} > 0.94''$. 464 galaxies were selected for ROTCURVE fitting. Of these 445 also had ACS imaging and ellipticity/position angle data, and 380 of the rotation curve fits were judged to be good by visual inspection.

ROTCURVE fits to a single emission line for each object. It first fits an emission line to data in each row of pixels, using a similar algorithm to LINEFIT, to obtain profiles of velocity and dispersion along the slit, and rejects rows with discrepant values using automatic criteria, testing for e.g. large row-to-row jumps. It measures the light distribution along the slit of the continuum plus emission, fits a gaussian to this profile, and subtracts the assumed seeing (here $0.7''$) in quadrature to determine the intrinsic, unblurred intensity profile, modeled as a gaussian $G(x)$ with dispersion r_I . A minimum $r_I = 0.2''$ is imposed to keep intrinsic profiles of small objects from becoming pointlike.

About half the TKRS masks have seeing $= 0.7''$ and the remainder have seeing up to $1.0''$, determined from the spectra of identified stars and the distribution of fitted widths of galaxies. Assuming a smaller seeing than the actual leads to a small underestimate of V_{rot} . Assuming a larger seeing than the actual causes the ROTCURVE modeling to fail on small objects, because it derives a too-small intrinsic spatial extent r_I , and the rotation velocity is poorly constrained due to the assumed large seeing blur.

ROTCURVE then constructs models of the intrinsic position-velocity distribution along the slit. The velocity model is an arctangent rotation curve centered at the peak of continuum+emission light, with a spatially-constant velocity dispersion, so that the intensity in position-velocity space before blurring by seeing and instrumental resolution is:

$$I(x, v) = G(x) \exp\left(-\frac{(v - V(x))^2}{2\sigma_{2d}^2}\right), \quad (2)$$

$$G(x) = \frac{I_{\text{tot}}}{\sqrt{2\pi}r_I} \exp\left(-\frac{(x - x_0)^2}{2r_I^2}\right), \quad (3)$$

$$V(x) = V_{\text{rot}} \frac{2}{\pi} \arctan(x/r_v). \quad (4)$$

$G(x)$ is the intrinsic gaussian light distribution along the slit. $V(x)$ is the rotation curve with asymptotic circular velocity V_{rot} and knee radius r_v , and σ_{2d} is the velocity dispersion, assumed constant along the slit. For the case of the [O II] 3727 doublet, we use a double gaussian for the distribution in velocity, with intensity ratio 1.4.

The unblurred $I(x, v)$ is then blurred for seeing with a 1-d gaussian in the spatial direction. The seeing has the effect of mixing gas at different velocities together, smoothing out velocity gradients and increasing the observed velocity dispersion at gradients (see Section 4.2 for an illustration of this effect). ROTCURVE then takes

moments of the blurred $I_{\text{blur}}(x, v)$ in the velocity direction to produce a model rotation curve and dispersion profile, and computes χ^2 of the data–model. It also fits for an offset in velocity since the published redshifts can vary from the systemic velocity, especially when there are large velocity gradients.

The model parameters that can be varied are V_{rot} , σ_{2d} , and r_v . For each galaxy, we construct a grid of models over V_{rot} and σ_{2d} . Because the models are fairly simple and involve a series of 1-d convolutions, a brute-force minimization is practical; the minimum in χ^2 on the grid is always unambiguous and well localized. The best-fit values of σ_{2d} are near-quantized in units of the grid spacing (here 5 km s^{-1}) due to the minimum-finding technique we used.

The rotation scale length r_v , describing how fast the rotation curve rises, is not strongly constrained by the ROTCURVE approach due to the seeing blur and the lack of 2-d modeling and position angle information. We chose a fixed $r_v = 0.2''$ for all galaxies, which can fit most rotation profiles; $0.1''$ and $0.3''$ fit worse for most galaxies. The knee radius and circular velocity are moderately covariant because the rotation curve turnover is not well resolved; changing r_v from $0.2''$ to $0.1''$ or $0.3''$ changes V_{rot} by about 0.1 dex in the mean; larger r_v causes larger V_{rot} . The effect on V_{rot} caused by assuming $0.5''$ or $0.9''$ seeing is about 0.05 dex. The combination of V_{rot} and σ_{2d} in quadrature, discussed in Section 5.2 below, changes by only half as much as V_{rot} .

Figure 1 shows ACS *I*-band images of four example galaxies at $z \sim 1$ from the TKRS. Figure 2 shows postage stamp images of their emission line spectra, and Figure 3 shows their rotation and dispersion profiles fit by ROTCURVE. In Figure 3, the points are velocity and dispersion from the spectra; the dashed and solid lines show the best-fit model before and after applying the seeing blur. These galaxies are relatively clean examples of a dichotomy in kinematic profiles that is common in the TKRS data.

TKRS 2021 and 3168 show the familiar shape of a rotation curve. Beam smearing by the seeing not only smooths out the gradient in velocity, but induces a peak in the observed dispersion; the intrinsic dispersion is significantly less than the observed. TKRS 5627 and 10023 are less familiar. They have quite small rotation, but require a velocity dispersion component to fit the data, with $\sigma_{2d} > V_{\text{rot}}$. Galaxies like TKRS 5627 and 10023 are common in our sample and are the reason we formulated ROTCURVE to include the velocity dispersion σ_{2d} as a second free parameter in the modeling. Note that these galaxies are relatively small but not extreme starbursts; they are not compact, nor very faint. We discuss rotation and dispersion dominated galaxies further in Sections 5.1 and 6 below.

We rarely see a rotation curve in which the observed points clearly roll over onto the flat part of the rotation curve, especially at $z \gtrsim 0.4$. This is partly due to the limited extent of the data, but frequently a more important effect is the seeing blur, which makes the observed rotation curve rise shallower than the true rise. The effect seen in TKRS 3168 in Figure 3 is common: the de-blurred model rotation curve has neared its asymptotic value while the observed data are still rising. Despite the lack of a flat-part in the observed data, the fitted

values faithfully represent the observed velocity spread. Objects in which the data covered only a small spatial extent and the fitted velocity extrapolated beyond the data were rejected as erroneous fits.

Because the rotation curve data points are highly correlated, χ^2 does not yield errors on V_{rot} and σ_{2d} directly. The fitted velocity V_{rot} is a good representation of the gradient seen in the rotation curve, but subtler details such as the true errors on V_{rot} and its dependence on the spatial extent of the data will require further Monte Carlo simulation. Here and in Paper II, measuring Tully-Fisher evolution with V_{rot} and σ_{2d} is secondary to using them to probe the nature of galaxy kinematics, and as a test of the meaning of integrated linewidth σ_{1d} .

As a check on the fits and models, ROTCURVE uses the observed row-by-row-fit rotation velocity and dispersion profile to reconstruct the 2-d data, and subtracts it from the original data to produce a residual map. It also produces reconstructed 2-d data from the best-fit blurred model (convolving back to the instrumental resolution). The reconstruction from the row-by-row fits is generally very good. The reconstruction from the model is also generally good, although it leaves residuals in cases such as an asymmetry in emission intensity, since the model is symmetric by construction. In principle, the models could be fit directly to the 2-d data without ever reducing to a 1-d rotation curve, but the rotation curve is a useful tool for evaluating the data and model.

The ROTCURVE fitting procedure runs automatically. Afterwards we inspected the rotation and dispersion profiles to reject bad or erroneous fits. 380 of the 445 galaxies passed this inspection. The dominant causes of failures are: discrepant points in the rotation curve which evade ROTCURVE’s automatic rejection; asymmetry which offsets the photometric center from the kinematic center; or small spatial extent of the rotation curve: we rejected most objects for which the usable rotation curve data spanned less than $1''$.

ROTCURVE departs from previous high-redshift rotation curve modeling by making the velocity dispersion σ_{2d} a free parameter; to our knowledge, other models have all fixed the dispersion to some low value. Fixing the dispersion is probably acceptable for samples of only morphologically-normal inclined disk galaxies observed with well-aligned slits, where rotation is the chief kinematic support and is unambiguously detected. However, as seen for TKRS 5627 and 10023 and shown in Section 5.1, there are galaxies with low rotation and large dispersion in our broader sample, and for these, fitting without a dispersion term will yield erroneous rotation velocities.

The dispersion term σ_{2d} in ROTCURVE does not have to correspond to a literal gas velocity dispersion similar to the velocity dispersion of stars in a spheroidal galaxy. Because we are measuring nebular emission lines that occur in gas at $T \sim 10^4 \text{ K}$, the gas in any individual H II region will have a dispersion of only $8\text{--}10 \text{ km s}^{-1}$. Taken literally, a dispersion $\sigma_{2d} \sim 30 \text{ km s}^{-1}$ implies a gas temperature of $T \sim 10^5 \text{ K}$, which is an unfavorable place on the ISM cooling curve. It is more likely that the dispersion comes from relative velocities of discrete H II regions.

Values of $\sigma_{2d} \gtrsim 20 \text{ km s}^{-1}$ can represent an effective dispersion, caused by the blurring of velocity gradients on scales at or below the seeing limit. Such a seeing-induced

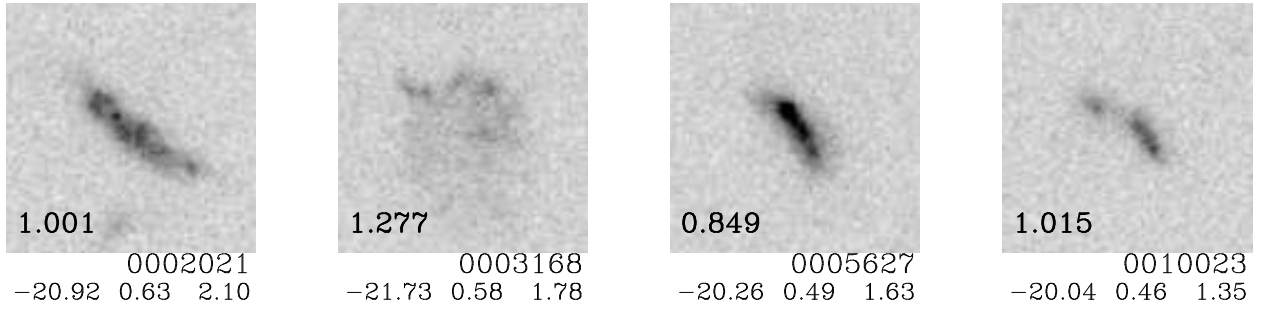


FIG. 1.— ACS *I*-band images for the example galaxies whose rotation and dispersion are shown in Figure 3: TKRS 2021, 3168, 5627, and 10023. The images are $3''$ on a side; north is up and west is to the right. The panels are labeled with redshift (in the image), TKRS ID, restframe M_B , $U - B$, and linewidth $\log \sigma_{1d}$. The DEIMOS slit PAs are 51° , 14° , 37° , and 39° respectively, north through east. The galaxies were classified as edge-on, LSB/irregular, chain, and hyphen/chain morphology, respectively.

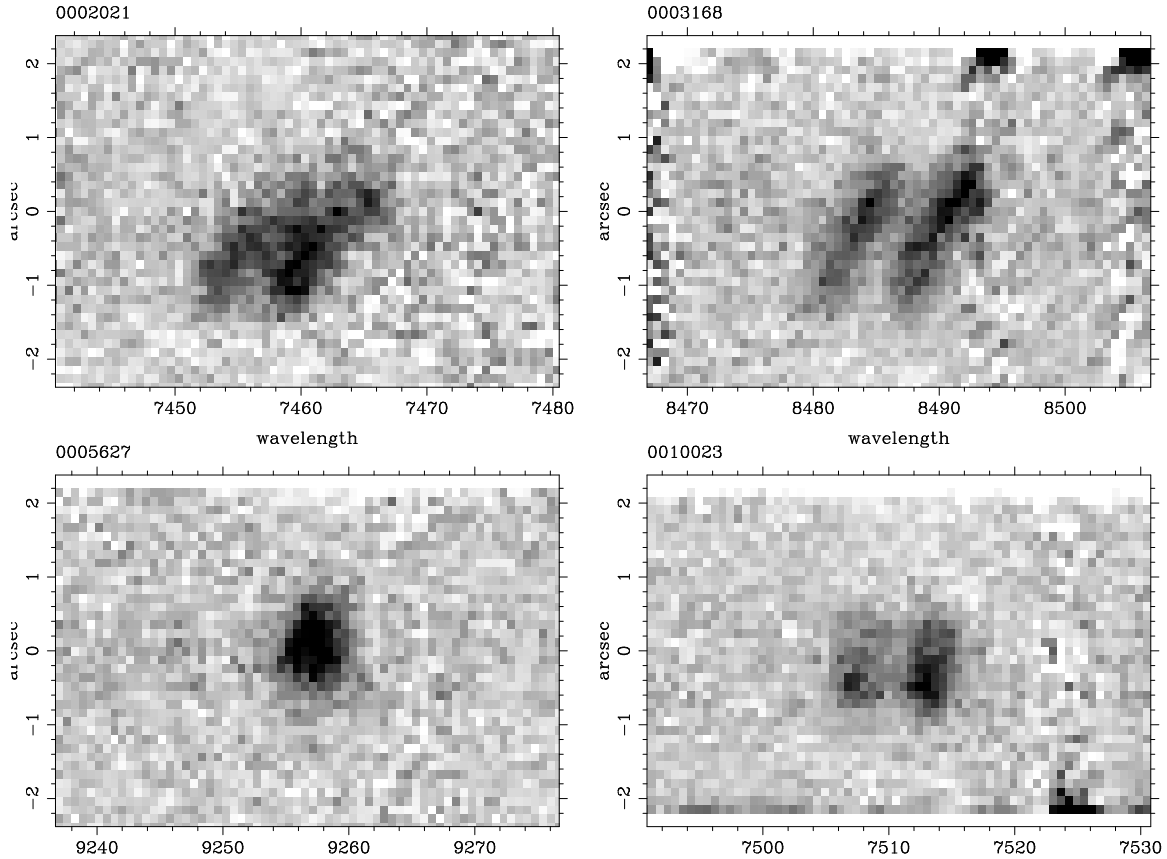


FIG. 2.— Postage stamps of the DEIMOS spectra for the example galaxies whose rotation and dispersion are shown in Figure 3: TKRS 2021, 3168, 5627, and 10023. The spectra have been sky-subtracted, and rectified for display purposes so that columns are constant wavelength. The galaxy continua, at low S/N/pixel, are not visible in these postage stamps. Each image shows the emission line used for ROTCURVE fitting, the [O II] 3727 doublet for 2021, 3168, and 10023, and [O III] 5007 for 5627. TKRS 2021 and 3168 show tilted emission lines, the signature of rotation curves, but TKRS 5627 and 10023 show very little velocity gradient.

dispersion σ_{2d} can appear for slits which are aligned close to the minor axis of the galaxy and miss the resolved velocity gradient, as shown in Section 4.2. But for TKRS 5627 and 10023, and similar galaxies in our sample, the slit was well aligned with the photometric major axis, yet there is almost no ordered velocity gradient. The effective dispersion σ_{2d} must be explained by non-ordered or disturbed gas kinematics on angular scales well below the seeing blur; these motions may not even have a preferred plane. The geometry of the H II regions, and why

they have not dissipated into a rotating disk, cannot be measured with these seeing-limited observations.

2.4. Photometry

Nearly all TKRS galaxies have *BViz* photometric measurements from the GOODS ACS catalog (Gavalisco et al. 2004). Ground-based photometry in *UBVRiz'*(*HK'*) for a large field including GOODS-N is available from Capak et al. (2004). We used the $2.8''$ diameter aperture magnitudes from the GOODS cata-

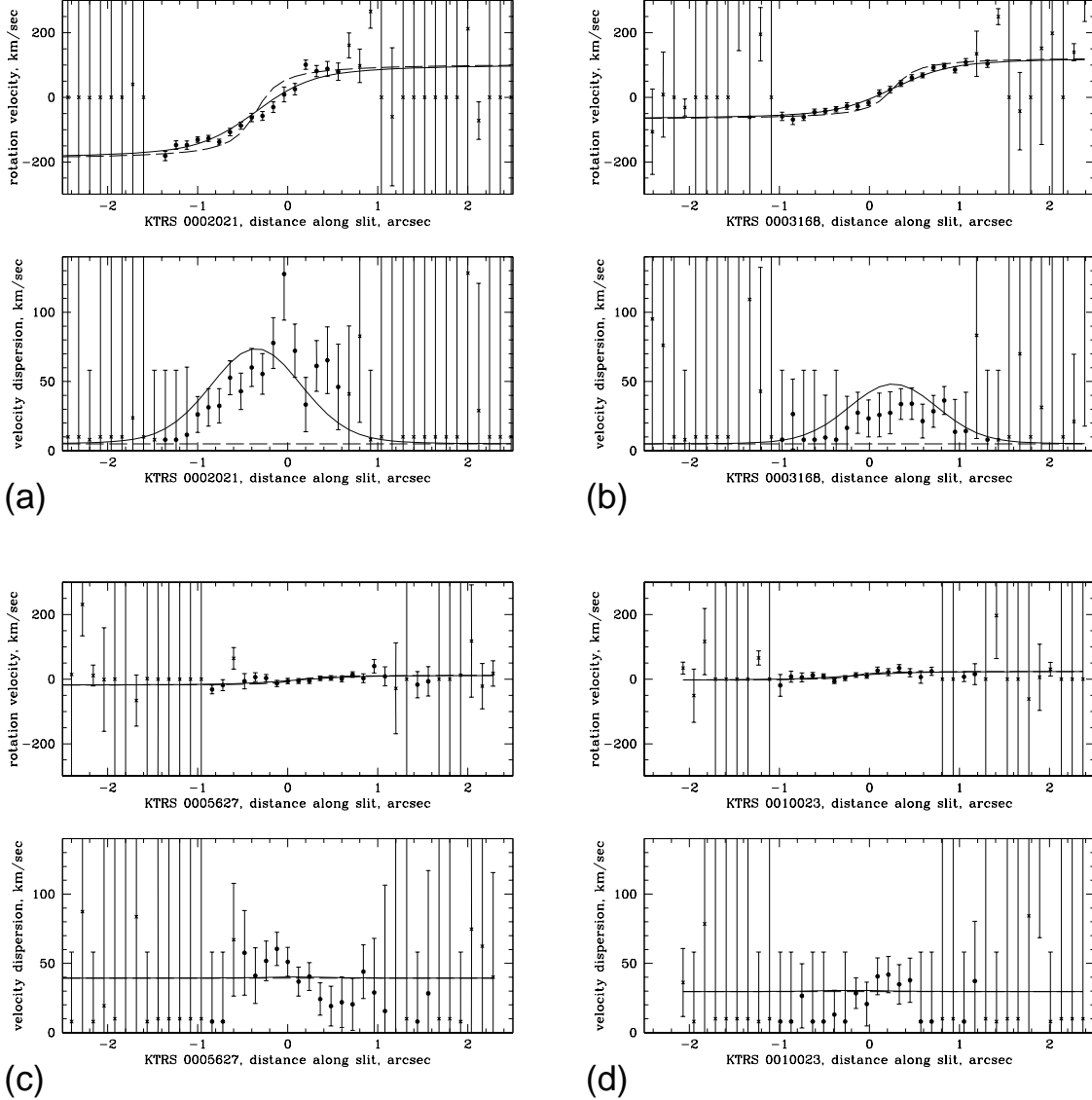


FIG. 3.— Rotation and dispersion profiles for four example galaxies with well aligned slits. TKRS 2021 and 3168 at $z = 1.00$ and 1.28 are rotation dominated; TKRS 5627 and 10023 at $z = 0.85$ and 1.02 are dispersion dominated. The slit PA offsets are 6° , 9° , 3° , and 10° . The points are the observed rotation and dispersion along the slit; filled circles are the data used by ROTCURVE while crosses were rejected by the program. The dashed curves show the intrinsic rotation and dispersion model profiles, and solid curves are the models after the seeing blur is applied. In panels (c) and (d) the solid curve overlies the dashed curve. The fitted rotation velocities and dispersions are $V_{rot} = 149, 97, 16, 14 \text{ km s}^{-1}$ and $\sigma_{2d} = 5, 5, 39, 30 \text{ km s}^{-1}$ respectively.

log and the $3''$ diameter magnitudes from the Capak catalog. For all but the largest, lowest-redshift galaxies, aperture corrections are small, so we omit them. Of the 1440 TKRS galaxies, 1423 have matches with optical magnitudes in the Capak et al. catalog. Fourteen of the remainder have magnitudes from the GOODS ACS catalog, and only 3 have neither.

The Capak et al. HK' data are shallower than the optical data and the depth is not constant over the GOODS field. We used only aperture HK' magnitudes that have errors < 0.3 mag, yielding HK' for 919 TKRS galaxies. With this error cut, the fraction of TKRS galaxies with HK' magnitudes reaches 50% at $HK' = 22.3$ (AB).

Our primary interests are to measure consistent rest-

frame absolute blue magnitude M_B and color $U - B$, and a rest infrared magnitude M_J and $R - J$ color. We convert to rest B and J because the observed filters cover or come relatively close to these restframe bands over $0 < z < 1.5$, minimizing extrapolation. We used the template-fitting K -correction procedure described in previous DEEP papers (Weiner et al. 2005; Willmer et al. 2006) to convert observed colors into K -correction and restframe color. Briefly, this method uses redshifted templates: 34 spectra of local galaxies with wavelength coverage $1200\text{\AA} - 1 \mu\text{m}$ (Kinney et al. 1996) for M_B and $U - B$; and 9 templates generated by PEGASE (Fioc & Rocca-Volmerange 1997) representing E, Sb and Sd SEDs at 1, 5, and 10 Gyr for M_J and $R - J$. To analyze,

for example, a galaxy at $z = 0.8$ with $R - I = 1.2$, the templates are redshifted to $z = 0.8$ and their observed $R - I$ colors synthesized. Since the templates' restframe $U - B$ colors and K -corrections from I to B are known, we fit a low order polynomial to $U - B$ as a function of $R - I$ and evaluate this fit at $R - I = 1.2$ to find $U - B$ for the galaxy under analysis.

This procedure works best when the observed filter pair transforms relatively closely to the wavelength of the restframe filters, as is the case for $R - I$ at $z = 0.8$ into rest $U - B$. When the transformation is not close, there is larger scatter about the fit of $U - B$ as a function of observed color, so choosing an appropriate filter pair is important.

To derive the restframe $U - B$ and M_B presented here, we used the filter pairs of Capak $B - V$, $R - I$, and $I - z$, switching over from one pair to the next at $z = 0.6, 1.1$ respectively. For $\Delta z = 0.1$ around the switchover redshift we interpolate to make a smooth transition. For rest $R - J$ and M_J we use the observed $I - HK'$ filter pair and the HK' magnitude.

In practice, the K -corrections are fairly stable. However, certain filter pairs produce discordant results for restframe colors: e.g. ACS $B - V$ and $V - i$ produce colors for galaxies at $z = 0.5$ that are ~ 0.1 mag offset. This problem is most obvious with the ACS filter pairs and with the Capak $V - R$ color. In general, a warning sign of the problem shows up as template mismatch in a color-color plot: for certain combinations of redshift and color pairs, galaxies and redshifted templates do not fall on exactly the same locus. The reasons for these mismatches are not clear; they may be a combination of small zeropoint shifts and imperfect filter/instrument response curves. The effect is small on absolute magnitudes, and relative color measurements at a given redshift are reliable, but measurements of absolute color evolution over a large range in redshift can be affected.

We found that using the Capak $B - V$, $R - I$, $I - z$ color sets minimizes the effect of these mismatches; using the ACS filters produces slightly abnormal trends in restframe color with redshift. Comparing the absolute magnitudes and colors from the Capak color sets and from the fully independent ACS $B - V$, $V - i$, $i - z$ sets, we find that 95% of the objects have a magnitude difference < 0.33 and a color difference < 0.26 , yielding 1σ errors of 0.12 in M_B and 0.09 in $U - B$. The errors on observed optical magnitudes from Capak et al. (2004) are 0.05-0.07 mag at the TKRS limit; additional scatter is propagated into the absolute magnitudes by the observed color error and the template scatter in the K -correction procedure.

The median error on HK' magnitude for galaxies with kinematic measurements is 0.14 mag. Although we are using model rather than empirical SEDs to K -correct the IR magnitude, galaxy SEDs have less variety in the IR than the optical and so the K -correction depends only weakly on the specific templates used. The error on the IR observations dominates over the IR template scatter.

3. SAMPLE MAGNITUDE, COLOR AND COMPLETENESS

Of the 1440 TKRS galaxies, 1423 have magnitudes from Capak et al. (2004) and 14 have magnitudes from ACS (Giavalisco et al. 2004). 893 galaxies have magnitudes and a linewidth determination, and an additional

196 are kinematically unresolved. Of these 1089, 913 are brighter than $M_B = -18$, a limit we impose for Tully-Fisher fitting in Paper II. 681 of the 1089 with kinematics have a reliable M_J and 647 of these are brighter than $M_J = -19$. Table 2 lists TKRS galaxies, positions, redshifts, observed magnitudes, restframe magnitudes and colors, and linewidths.

Figure 4 shows the restframe optical color-magnitude distribution of TKRS galaxies and the location of the 1089 galaxies with and 348 without measured linewidths. The TKRS galaxies exhibit the color bimodality now well-established locally and to $z \sim 1$ (Strateva et al. 2001; Bell et al. 2004; Wirth et al. 2004; Weiner et al. 2005). Both red and blue galaxies show a shallow color-magnitude relation: brighter galaxies are redder in the mean. The majority of galaxies for which we fail to get a good linewidth are on the red side of the bimodality, $U - B > 0.95$, because those galaxies have weak or no emission lines (e.g. Weiner et al. 2005). Among the blue galaxies, linewidth failures are rare and fairly randomly distributed. We examined each failure and found that most are due to low line flux or night sky residuals. The failure rate in blue galaxies is small and there is no evidence that failures occur preferentially at large or small dispersions.

At low redshift, blue galaxies in the TKRS sample show the well-known color-magnitude relation; fainter galaxies are bluer (upper left panel of Figure 4). At higher redshift, the faint limit is due to the TKRS magnitude selection; the selection limit in apparent R magnitude corresponds to a tilted line in the restframe $M_B, U - B$ plane (e.g. lower left panel of Figure 4). The tilt of this line changes with redshift. In Paper II we test the effect of the selection limit on Tully-Fisher relations by defining an approximately mass-matched sample, applying the $z \sim 0.9$ tilt at all redshifts and a magnitude cut that evolves similarly to L^* . This cut is shown by the diagonal lines in Figure 4.

The redshift completeness of the TKRS is $\sim 70\%$ to $R_{AB} = 24.4$, discussed by Wirth et al. (2004). Redshift failures in the TKRS are mostly faint blue galaxies that are probably at $z > 1.5$. Here we discuss the linewidth completeness, i.e. the fraction of galaxies with good linewidths over galaxies with redshifts.

Figure 5 shows the linewidth completeness as a function of rest $U - B$ color. The completeness is roughly constant for blue galaxies but drops sharply for red galaxies. Because red galaxies are bright, a histogram of completeness as a function of rest M_B for the whole sample actually drops at bright magnitudes.

Red galaxies and blue galaxies are two distinct populations and the bulk of our measurements are blue galaxies, so in this paper we are constraining the behavior of the blue galaxy population. Figures 6 and 7 show the linewidth completeness of the sample restricted to TKRS galaxies on the blue side of the color bimodality, $U - B < 0.95$. Linewidth completeness is nearly constant with either absolute or apparent magnitude, with a small tendency to be lower for galaxies bright in absolute magnitude (lower emission EW) or faint in apparent magnitude (lower apparent flux). The lack of any strong dependence on magnitude reflects the fact that intrinsically-faint galaxies tend to have high emission equivalent width.

TABLE 2
CATALOG OF TKRS GALAXIES AND LINEWIDTH MEASUREMENTS

TKRS ID	Capak ID	RA (2000)	Dec (2000)	z^1	B^2	R^2	I^2	HK'^2	error ² (HK')	M_B^3	$U - B^3$	M_J^3	$R - J^3$	$\log \sigma_{1d}^4$
0000034	-99.9	189.019492	62.261711	0.4581	-99.90	-99.90	-99.90	-99.90	-99.90	-99.99	-99.99	-99.90	-99.90	1.648
0000117	59102	189.232904	62.360603	0.5852	24.71	23.66	23.34	22.33	0.36	-18.46	0.47	-19.88	0.69	1.483
0000225	62458	189.178462	62.333772	0.8547	24.49	24.09	24.08	-99.90	-99.90	-19.08	0.07	-99.90	-99.90	1.621
0000239	45551	189.084525	62.291556	0.8480	25.10	23.66	22.70	20.97	0.11	-20.37	0.90	-22.27	0.91	1.879
0000241	62192	189.197325	62.342981	0.8894	24.29	23.84	23.12	-99.90	-99.90	-20.12	0.68	-99.90	-99.90	1.357
0000276	58390	189.292225	62.386944	1.2590	24.23	23.56	23.15	-99.90	-99.90	-21.58	0.77	-99.90	-99.90	-99.900
0000320	63030	189.136354	62.312436	0.4826	24.81	24.11	23.88	-24.14	0.87	-17.41	0.29	-99.90	-99.90	1.400
0000345	50539	188.929450	62.215525	0.8509	24.41	23.66	22.97	21.58	0.37	-20.10	0.65	-21.64	0.80	-99.900
0000428	58669	189.274379	62.375206	0.4870	24.31	23.78	23.53	-24.26	2.01	-17.87	0.26	-99.90	-99.90	1.400
0000432	62868	189.150483	62.318058	0.6809	23.83	22.48	21.88	20.87	0.06	-20.44	0.65	-21.72	0.66	1.874
0000444	46466	189.006417	62.253725	0.2985	23.44	22.07	21.72	21.15	0.19	-18.19	0.74	-19.44	0.45	1.499
0000445	62021	189.214375	62.348203	0.7441	23.58	22.77	22.25	21.45	0.22	-20.40	0.53	-21.33	0.46	1.650
0000448	59290	189.223667	62.353142	0.4724	23.14	22.08	21.83	20.98	0.14	-19.54	0.58	-20.71	0.60	1.693
0000463	62992	189.143487	62.313794	0.5027	24.66	23.87	23.66	22.56	0.24	-17.67	0.31	-19.29	0.77	1.579
0000484	-99.9	189.171067	62.326453	0.6088	23.96	-99.90	23.06	-99.90	-99.90	-19.07	0.39	-99.90	-99.90	1.400
0000555	46181	189.033342	62.264919	0.4589	23.21	21.88	21.58	20.89	0.24	-19.66	0.73	-20.72	0.47	1.885
0000584	46681	188.998854	62.246286	0.5306	23.85	22.55	22.23	21.31	0.21	-19.23	0.61	-20.67	0.64	1.400
0000593	58521	189.284400	62.381100	0.2046	24.31	23.66	23.51	23.44	0.99	-15.86	0.36	-16.33	0.07	1.400
0000617	46339	189.025129	62.258847	0.4542	23.68	22.58	22.41	22.18	0.38	-18.90	0.58	-19.41	0.17	1.274
0000618	58908	189.266258	62.368506	1.0080	24.36	23.92	23.18	22.64	0.73	-20.59	0.78	-20.81	0.19	1.488

NOTE. — The complete version of this table is in the electronic edition of the Journal. The printed edition contains only a sample. Undefined values are given as -99.900.

¹Redshift.

²Apparent $BRI(HK')$ AB aperture magnitudes (Capak et al. 2004). Galaxies with only BI use GOODS ACS aperture magnitudes (Giallisco et al. 2004).

³Restframe M_B , $U - B$, M_J and $R - J$ AB magnitudes from the SED K correction procedure described in text.

⁴Log linewidth in km s^{-1} from integrated emission and its error. Galaxies assigned a log linewidth of 1.4 and error of 0.2 are kinematically unresolved, see text.

Because completeness of the linewidth sample depends strongly only on color, we have a fair sample of the blue galaxy population, and our measurements will not be strongly affected by selection effects. Of course, any evolution measurement or interpretation will apply only to blue galaxies.

4. PROPERTIES OF KINEMATIC MEASURES

The limited spatial resolution of high-redshift spectra makes the interpretation of kinematic measures less obvious than in local galaxies. Our goal in this section is to establish the properties of our sample and determine the effect of observational limitations on the measures of dispersion and rotation.

There has been some controversy over how well measures such as integrated linewidth probe galaxy kinematics. Modeling simulated observations of disk velocity fields with true circular velocity V_c , Rix et al. (1997) found that for their observational parameters, the average integrated linewidth $\langle \sigma \rangle / V_c = 0.6$ with substantial scatter (~ 0.15) depending on the unknown position angles and inclinations, where $\langle \sigma \rangle$ incorporates an average over inclination but V_c is the true value. For random orientations, $\langle \sin i \rangle = 0.79$, leaving an average factor of 0.76 for $\sigma / (V_c \sin i)$. From observations of local galaxies, Kobulnicky & Gebhardt (2000) found that the [O II] emission linewidth tracks the H I linewidth W_{20} well for most galaxies, using $\sigma = 0.28W_{20}$ (both uncorrected for inclination), but the [O II] linewidth is low in 2/22 extreme cases. (The H I width W_{20} is the full-width of the H I profile at the 20% flux level.) This relation is roughly consistent with the Rix et al. relation since $W_{20} \simeq 2(V_c \sin i + 15 \text{ km s}^{-1})$ (Tully & Fouque 1985).

Lehnert & Heckman (1996) showed a tendency for

edge-on IR-luminous starburst galaxies to have nuclear emission linewidth that is low compared to the expected velocity dispersion of the full potential; these galaxies are mostly fairly large and the nuclear emission does not probe the full potential. Barton & van Zee (2001) observed four blue compact dwarf galaxies and found that $\sigma(\text{H}\alpha)$ falls below optical V_{rot} and H I W_{50} . However, their four galaxies average $\sigma/V_{2.2} = 0.7$, and the two with 21 cm data have $\sigma/W_{50} = 0.27$ (all quantities uncorrected for inclination). These are actually fairly consistent with the $\langle \sigma \rangle / V_c$ offset of Rix et al. and the linewidth / H I width factor of Kobulnicky & Gebhardt. Rotation curves can also be affected: kinematic distortions and truncations could cause galaxies to have low measured rotation (Barton et al. 2001; Kannappan & Barton 2004).

Perhaps the most serious discrepancy between optical and H I width is found in a sample of 10 local blue compact galaxies (BCGs; Pisano et al. 2001), which show $W_{20}(\text{H}\beta)/W_{20}(\text{H I}) = 0.66 \pm 0.16$. In terms of dispersion this implies $\sigma(\text{H}\beta)/W_{20}(\text{H I}) = 0.18$. These galaxies are a fairly special population with high emission equivalent widths and small sizes, $r_e = 0.6 - 1.9$ kpc, smaller than average for intermediate- z BCGs. They are most similar to NGC 4449, the furthest outlier in the sample of Kobulnicky & Gebhardt (2000), which has a much larger H I extent than optical; and to the compact narrow emission-line galaxies (CNELGs, Koo et al. 1995) in their sizes. In the sample of Pisano et al., the optical linewidths are most affected when $W_{20}(\text{H I}) < 150 \text{ km s}^{-1}$, which corresponds to an unaffected optical $\sigma < 45 \text{ km s}^{-1}$; smallest galaxies can be the most seriously affected.

These types of underestimation of kinematic width may happen in high-redshift samples. They might ex-

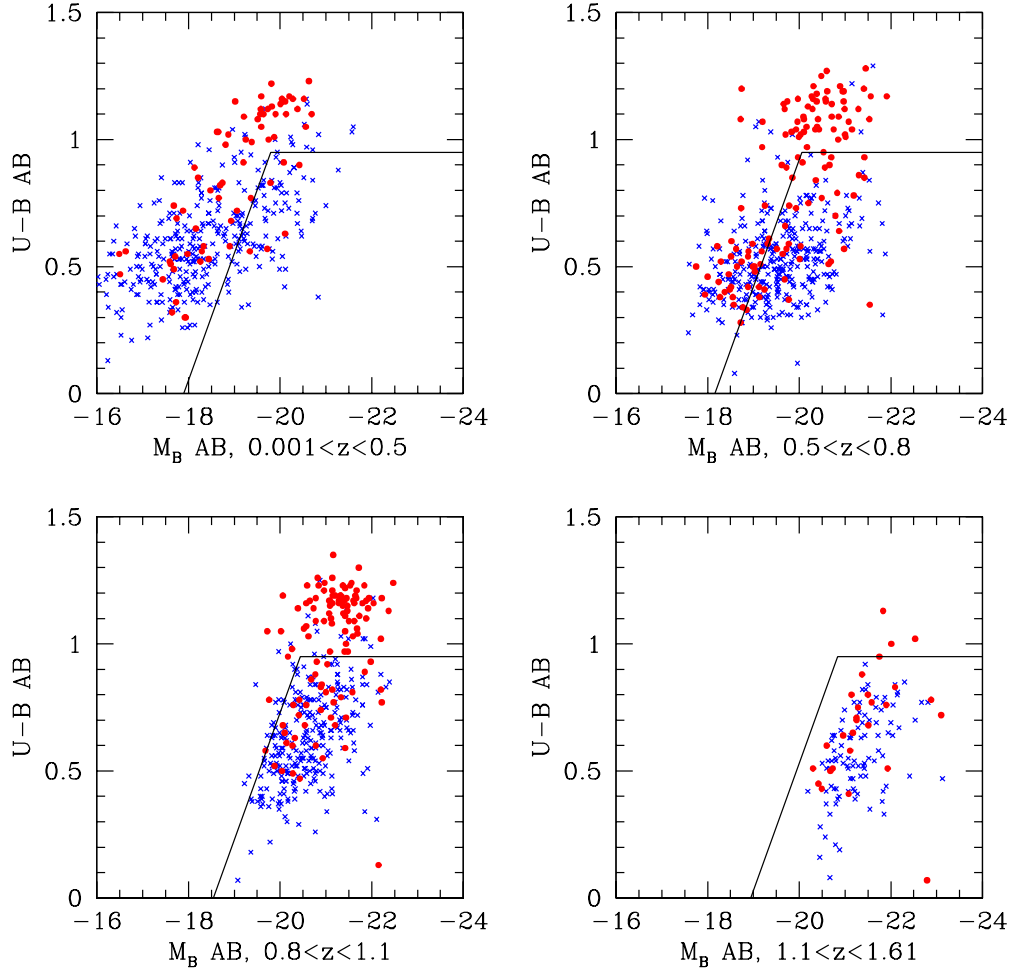


FIG. 4.— Absolute magnitude and color for TKRS galaxies in 4 redshift ranges. Blue Xes: galaxies with good linewidths; red circles: galaxies with poorly measured linewidth. The bulk of linewidth failures are in the red side of the color bimodality. The horizontal and diagonal lines show a magnitude and color selection that constructs samples whose depth is matched to the selection limit at $z = 0.9$ and an evolving L^* .

plain some of the discrepancies between previous TF evolution measurements, as Pisano et al. (2001) suggest, especially in samples with high line EW. However, even at high redshift, the extreme BCGs or CNELGs are a minority of blue galaxies (Koo et al. 1995). These galaxies are quite small; even with 1-2 mag brightening, the Pisano et al. (2001) sample would be among the faintest of the $z \sim 1$ galaxies in the TKRS sample. The possibility of BCG-induced offsets does argue in favor of using large samples which are not selected on emission line EW, and in which evolution can be measured internal to the sample.

Ideal measures of high-redshift kinematics would yield 2-d maps with high spatial resolution. This may soon be possible with adaptive optics and integral field spectroscopy, but will remain impractical for large samples for some time. Here we carry out empirical tests on our sample and simulations of seeing-blurred observations to test the properties of linewidth measurements.

4.1. Spatial extent of emission

It is frequently suggested that high-redshift galaxies could have enhanced emission from their centers, such as a nuclear starburst, and that this could produce smaller linewidths because the emission does not probe the full potential, or comes from a part of the rotation curve that is rising (e.g. Lehnert & Heckman 1996). Simard & Pritchett (1998) found that $\sim 25\%$ of their galaxies had unresolved emission in their CFHT spectra. Rix et al. (1997) suggested that $\sim 20\%$ of their sample might have nuclear emission from high-density gas, based on the [O II] doublet ratio. However, both of these samples are selected to have high EW or blue colors, and are relatively low S/N compared to the TKRS spectra. Another possibility is that line emission could be dominated by one or a few large HII regions and so not probe the full velocity field of the disk.

We tested the spatial extent of emission in the TKRS linewidth sample by fitting gaussian profiles along the slit. We collapsed the 2-d data in the wavelength di-

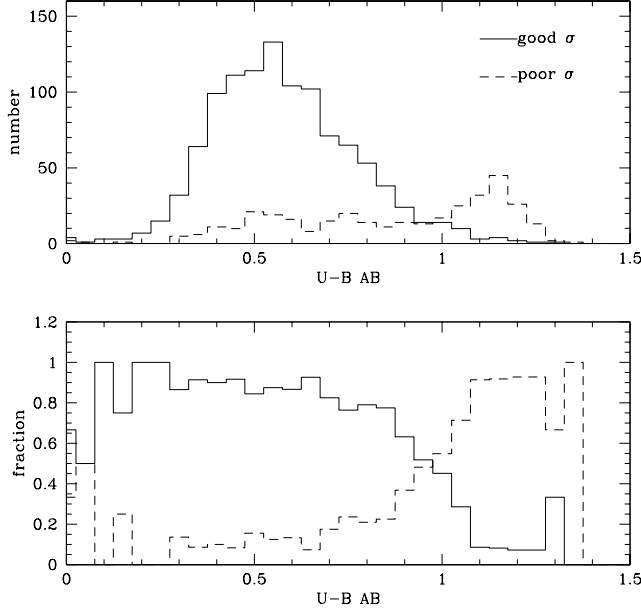


FIG. 5.— Linewidth completeness as a function of restframe $U-B$ color. Solid line: galaxies with good linewidths; dashed line: galaxies with poorly measured linewidth. The top panel shows absolute numbers and the bottom panel shows good or bad as a fraction of the total with redshifts.

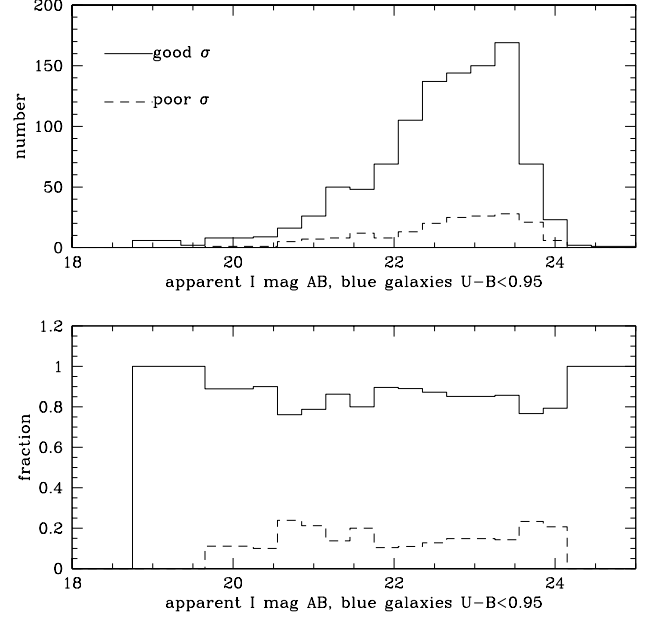


FIG. 7.— Linewidth completeness for blue galaxies as a function of apparent magnitude I_{AB} . Solid line: galaxies with good linewidth; dashed line: galaxies with poor linewidth measure. The top panel shows absolute numbers and the bottom panel shows good or bad as a fraction of the total of blue galaxies with redshifts.

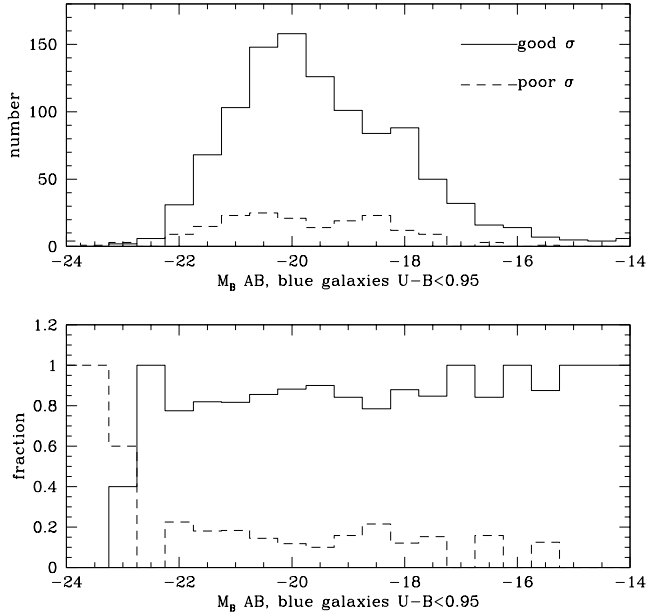


FIG. 6.— Linewidth completeness for blue galaxies as a function of absolute magnitude M_B . Solid line: galaxies with good linewidths; dashed line: galaxies with poorly measured linewidth. The top panel shows absolute numbers and the bottom panel shows good or bad as a fraction of the total of blue galaxies with redshifts.

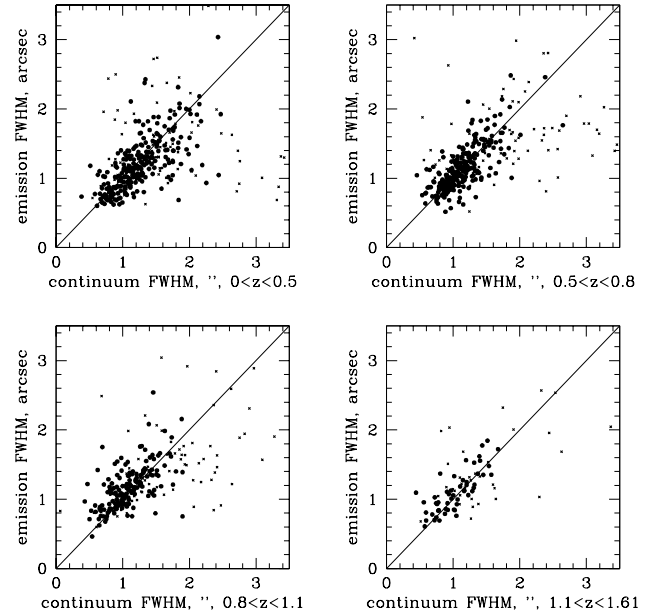


FIG. 8.— Spatial extent along the slit for TKRS galaxies in four redshift ranges. The fitted gaussian FWHMs of emission and continuum are plotted. Filled circles have error on both FWHMs $< 0.1''$, Small Xes have error on one or both FWHMs $> 0.1''$, indicating an unreliable fit. The sizes are seeing-limited around $\text{FWHM} \sim 0.7''$, and above that are consistent with equal sizes for emission and continuum.

rection over a 15 \AA range for emission and two 100 \AA ranges on either side of the line for continuum. We then

fit gaussians using a non-linear least squares routine.

The fitted spatial widths of emission versus continuum are shown in Figure 8, divided into four redshift ranges. The sizes are seeing-limited around $\text{FWHM} \sim 0.7''$ and track each other well at larger sizes. The small mask-to-mask seeing variations in the TKRS data will tend to spread galaxies along the 1:1 line, but the relation continues far beyond $\text{FWHM} \sim 1.0''$. Outliers from the 1:1 line generally have a large error in one size measurement. While this comparison is somewhat limited by seeing, there is no evidence for a large population of nuclear emission or single-HII-region emission. In fact there is strong evidence that emission and continuum size track each other well.

4.2. What integrated linewidths measure: simulation of observations

In order to understand what an integrated linewidth is really measuring, we simulated observations of a disk galaxy at $z = 1$, using an actual 2-dimensional intensity and velocity field from Fabry-Perot observations of the local galaxy NGC 7171. A similar project was carried out, also using Fabry-Perot velocity fields as input, by Rix et al. (1997). NGC 7171 has a fairly typical disk velocity field with mild spiral streaming motions, and abundant $\text{H}\alpha$ emission, yielding a 2-d velocity field that samples the disk well with high resolution. It was observed in the $\text{H}\alpha$ line with the Rutgers Fabry-Perot at the CTIO 4-m Blanco telescope, on October 27 and 28, 1989 by T.B. Williams and R.A. Schommer⁹. The data were reduced into intensity, velocity, and dispersion fields by BJW using procedures described elsewhere (Palunas and Williams 2000; Weiner et al. 2001) and have been previously studied by Palunas (1996). NGC 7171 has a heliocentric velocity of 2740 km s^{-1} and we assumed a distance of 34 Mpc; its magnitude is $M_B = -20.0$. The resolution of these 2-d maps is $1.5''$, the inclination of NGC 7171 is 55° , and its rotation velocity corrected for inclination is $V_c = 189 \text{ km s}^{-1}$. It has a flat rotation curve and lies on the Tully-Fisher relation of Sakai et al. (2000).

The original $\text{H}\alpha$ intensity, velocity and dispersion fields of NGC 7171 are shown in the left column of Figure 9; the dispersion field is relatively featureless since the dispersion is usually $< 20 \text{ km s}^{-1}$ except in the nucleus, where it is increased by seeing blur. We used these fields to reconstruct a 3-d spectral cube. To simulate an observation at $z = 1$, we rescaled to the angular size at $z = 1$, blurred each plane of the cube by a $0.7''$ gaussian to represent seeing, and resampled the cube onto DEIMOS pixels of $0.118''$. We then refit through the cube to produce maps of restframe intensity, velocity, and dispersion. The right column of Figure 9 shows the resulting $z = 1$ maps that correspond to the unblurred maps of the left column.

The blurred velocity and dispersion fields of Figure 9 illustrate an effect we alluded to in the discussion of rotation curve fitting in Section 2.3.2. The beam smearing due to seeing smooths out the rotation velocity gradient, but it produces a strong peak in the velocity dispersion in the center; where the unblurred velocity gradient is strong, the seeing mixes gas at different velocities to-

gether. This peak in velocity dispersion is at high $\text{H}\alpha$ intensity and so carries a high weight in integrated measurements.

We used blurred velocity cubes to simulate observations of integrated velocity dispersion over a range of galaxy inclinations and slit-galaxy relative position angle misalignments. To simulate a range of inclinations, we stretched the input NGC 7171 fields and rescaled the velocities before blurring and resampling. We did not allow the dispersion to fall below 8 km s^{-1} , a typical sound speed for H II regions and gas in the ISM. We did not add noise or scale the flux to a real galaxy, as this is not a full simulation of real observations, but a test of the relative contribution of emission at different velocities. Adding noise reduces the detectability of spatially resolved emission at low intensities but does not greatly affect the velocity distribution of the integrated emission.

We then laid down typical $1''$ wide slits over a range of relative PAs and extracted a spectrum in a $2.3''$ (1.5 FWHM) extraction window, using the intensities, velocities and dispersions of pixels within the slit and window to build up an emission spectrum. The resulting velocity profile can be somewhat non-gaussian and flat-topped, especially when the slit is aligned with the galaxy major axis, but once the profile is convolved with the spectrograph resolution, the non-gaussianity is small. We computed moments to determine the velocity dispersion corresponding to σ_{1d} . Changing the extraction diameter within reasonable limits had little effect on the results, because the bulk of the signal comes from the central emission peak.

Figure 10 plots the ratio of integrated linewidth to projected circular velocity, $\sigma_{1d}/(V_c \sin i)$, as a function of inclination and relative slit position angle. This ratio removes the $\sin i$ effect, isolating the properties of the integrated linewidth. There is a small residual effect of inclination, but the variation among the tracks is quite small. The exception is the nearly face-on $i = 5^\circ$ case, where the 8 km s^{-1} minimum dispersion contributes. The chances of observing a face-on, perfectly flat thin disk are very small, especially in the high- z universe where many galaxies are peculiar or irregular. Apart from this special case, the ratio varies by $\pm 15\%$ over the range of PA and inclination.

At a given inclination, the linewidth for misaligned slits is lower, but the linewidth for a perfectly misaligned slit ($\Delta PA = 90$) is only 20% lower than the linewidth for a perfectly aligned slit ($\Delta PA = 0$). The reason is that the observed linewidth comes largely from the central peak in intensity and dispersion, seen in the lower panel of Figure 9. The slit position angle does have a large effect on the observed rotation gradient, of course. Both these effects are seen empirically in our data in Section 4.4. The ratio $\sigma_{1d}/(V_c \sin i) \sim 0.6 - 0.65$ on average. When the distribution of inclinations is accounted for, the ratio is fairly similar to the distribution in Figure 7 of Rix et al. (1997): $\sigma_{1d}/V_c \sim 0.55$ in the mean, with a non-gaussian scatter due to the tail of nearly face-on model galaxies with low σ_{1d} .

The upshot of these simulations is that the seeing is a powerful integrator, smoothing over the disk and producing dispersion at the location of velocity gradients, so that specific observational parameters like slit PA, width, and extraction diameter do not have a strong effect on

⁹ Cerro Tololo Inter-American Observatory is operated by AURA under contract to the NSF.

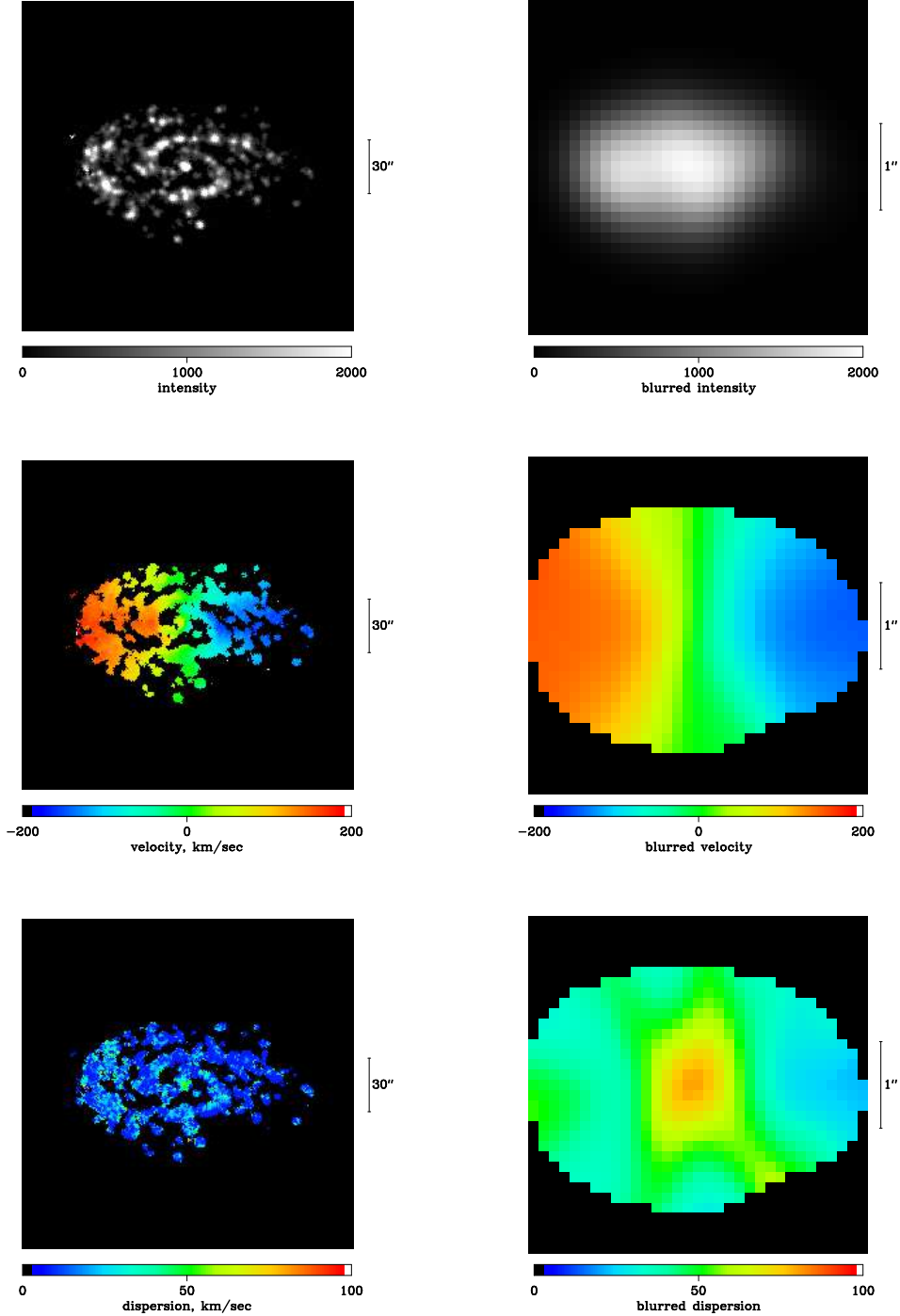


FIG. 9.— Emission intensity, line-of-sight velocity, and dispersion fields for NGC 7171 as observed locally (left column) and as it would be seen at $z = 1$ with $0.7''$ seeing and $0.118''$ DEIMOS pixels (right column). The scale bar is $30''$ on the left and $1''$ on the right. The velocity color scale is $\pm 200 \text{ km s}^{-1}$ and the dispersion color scale is $0\text{--}100 \text{ km s}^{-1}$. The seeing blur smooths out the rotation velocity gradient, but causes a central spike of dispersion where emission from gas at different velocities is superimposed.

the integrated linewidth. However, the slit PA does have a strong effect on the observed spatially-resolved rotation curve. Similar conclusions were reached by Erb et al. (2004). Inclination produces significant scatter in linewidth/velocity ratio merely through the $\sin i$ factor.

A limitation is that we have modeled only a thin disk galaxy in orderly and planar rotation. Our comparison

of observed rotation velocity and dispersion in Section 5.1 below shows that many galaxies are not dominated by orderly rotation. However, even if the kinematics are not orderly, the effect of the seeing as an integrator over the galaxy’s emission still operates. The net result is that the integrated linewidth is actually more robust than the rotation gradient against both unusual internal kinemat-

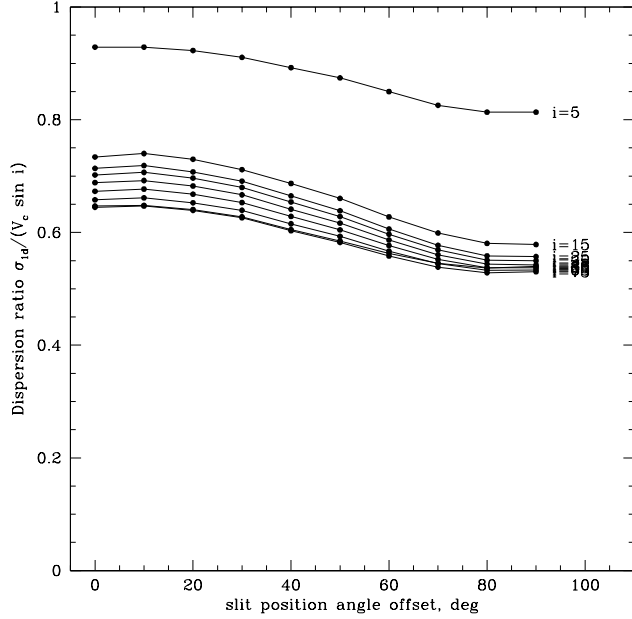


FIG. 10.— Ratio of integrated linewidth to projected circular velocity, $\sigma_{1d}/(V_c \sin i)$, as a function of inclination and slit position angle for simulated observations of NGC 7171 at $z = 1$. At a given inclination, the linewidth for a perfectly misaligned slit ($\Delta PA = 90^\circ$) is only 20% lower than the linewidth for a perfectly aligned slit ($\Delta PA = 0^\circ$). The ratio takes out the inclination dependence, showing that the effect of inclination other than through $\sin i$ is small. The exception is the $i = 5^\circ$ case, where the sound speed of the gas, 8 km s^{-1} , contributes to the observed linewidth.

ics and the observational effect of slit PA offsets.

If the star formation and emission is more centrally concentrated than in NGC 7171, the relative contribution of high velocity gas on the flat part of the rotation curve is reduced. However, because the central regions do have a velocity gradient, the integrated linewidth remains fairly high, and this is a second order effect. As a test, we artificially boosted the emission intensity inside 1 kpc radius – the central clump of emission – by a factor of 4 and reran the simulations. The integrated linewidth decreased by just $4.5 \pm 1\%$, over the range of inclination and slit PA. Centrally concentrated emission must overwhelm the rest of the galaxy to lower the linewidth significantly.

4.3. The effect of inclination corrections and the lack thereof

The modeling of a blurred NGC 7171 showed that the strongest effect on the observed integrated linewidth is the inclination factor of $\sin i$. Classic Tully-Fisher studies correlate velocity and luminosity after correcting for inclination and extinction, and are generally restricted to relatively high-inclination galaxies with clear disk geometry. In this study we do not restrict the sample. In large samples of high-redshift galaxies, correcting for inclination is only practical with HST imaging, and galaxies may have stronger deviations from an ideal thin circular disk geometry, so the relation between ellipticity and inclination is less direct. As groundwork for the Tully-

Fisher study of Paper II, here we model the effect on disk Tully-Fisher relations when inclination and extinction corrections are omitted.

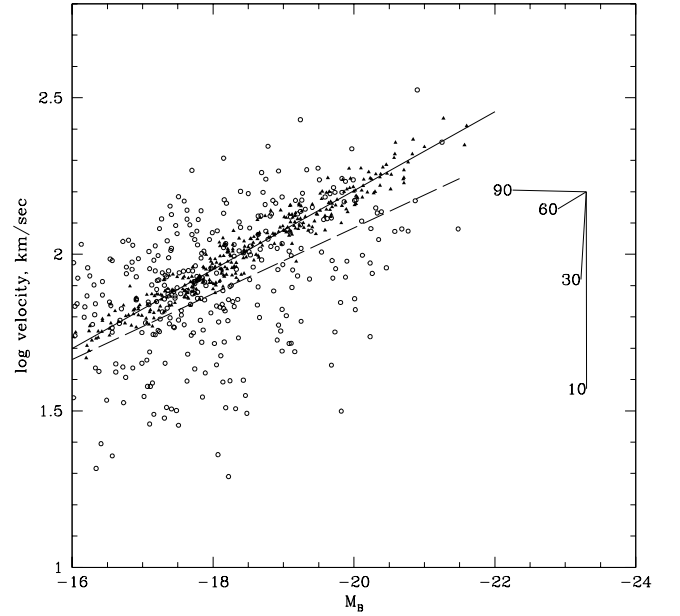


FIG. 11.— A simulated Tully-Fisher relation illustrating the effect of omitting inclination and extinction corrections. The black triangles are drawn from a Tully-Fisher relation with inverse TF slope -0.125 dex/mag and intrinsic scatter 0.0375 dex . The solid diagonal line is a linear fit to these points. The open circles are the same galaxies “observed” at randomly assigned inclinations i . The decorrelated quantities are velocities $V_{rot} \sin i$ with 0.084 dex observational error added and magnitudes $M_B + A_B(i)$ with 0.11 dex error. The dashed diagonal line is a linear fit to the decorrelated points. The lines at right indicate the deprojection tracks for a galaxy with $\log V_{rot} = 2.2$ at $i = 10^\circ, 30^\circ, 60^\circ, 90^\circ$. Edge-on galaxies move above the baseline inverse-TF relation due to extinction; face-on galaxies fall below the baseline due to low projected velocities. For B band extinction, galaxies at the median inclination $i = 60^\circ$ are nearly unchanged. However, the scatter around the TF relation becomes large and non-gaussian.

Figure 11 shows a model Tully-Fisher relation with and without inclination and extinction corrections. The filled triangles are a simulated “true” Tully-Fisher relation with a realistic distribution of magnitudes (drawn from our sample in $0 < z < 0.5$), an inverse-TF $\log V(M)$ slope of -0.125 dex/mag , and an intrinsic scatter of 0.0375 dex (0.3 mag). Each galaxy is assigned an inclination drawn from a uniform distribution in $\cos i$; we do not modify the inclination distribution to reflect the small bias against edge-on galaxies in a magnitude-selected sample, and surface brightness selection against face-on galaxies. The open circles are the decorrelated values $\log V_{rot,obs}$ and $M_{B,obs}$, with errors added from gaussian distributions of 0.084 dex and 0.11 mag . The extinction correction (to face-on) is $A_B = \gamma_B \log(a/b)$, with $\gamma_B = 1.57$ (Sakai et al. 2000, neglecting the luminosity dependence of extinction), and we assume the galaxies have intrinsic thickness:radius 1:5. The velocity is $V_{rot} \sin i$ with a random-motion component of 25 km s^{-1} added in quadrature, which prevents the face-on galaxies’ velocity from falling to near zero. The solid and

dashed lines show the best linear fits respectively to the original and decorrected points with $M_B < -18$ (using a fit method that compensates for scatter, described in Paper II). The fitted slopes are -0.126 ± 0.003 for the original sample and -0.105 ± 0.021 for the decorrected sample.

The lines at right show how decorrection moves a galaxy with $\log V_{rot} = 2.2$ for inclinations $10^\circ, 30^\circ, 60^\circ, 90^\circ$. The undoing of these inclination and extinction corrections moves the galaxies onto tracks nearly parallel to the original TF relation – e.g. all the $i = 90^\circ$ galaxies are shifted to fainter magnitudes, so appear above the original TF. For $\gamma_B = 1.57$ and a TF slope -0.125 , the corrections cancel at $i = 60.5^\circ$, which fortuitously is almost exactly the median inclination of $i = 60^\circ$ for a randomly oriented sample. Thus in B -band, the effect of undoing corrections on the TF intercept is relatively small. For the galaxies on a single inclination track, the slope is unchanged, but for the entire sample, the slope of the uncorrected inverse TF relation is shallower.

As shown in Figure 11, the scatter induced by lack of corrections is non-gaussian, although the non-gaussianity is blurred somewhat by the observational errors. The effect on Tully-Fisher fitting depends on the magnitude distribution and limit of the sample. The fitted TF relation changes due to the correlated anti-corrections scattering across the TF ridgeline, the non-gaussian scatter, and the elimination of edge-ons by the magnitude limit. For the realization shown here, a fit to the galaxies brighter than $M_{B,obs} = -18$ yields a velocity intercept shifted down by 0.11 dex at $M_{B,obs} = -20$, a slope of -0.105 ± 0.021 , and a greatly increased scatter of 0.19 dex. We emphasize that these values only apply for the idealized thin disk assumptions, which likely do not apply to many galaxies in the TKRS – for example, elongated but non-rotating galaxies like TKRS 5627 and 10023, shown in Figures 1 and 2.

Local Tully-Fisher samples require a luminosity or velocity-dependent extinction correction; extinction is higher in larger galaxies (Giovanelli et al. 1995; Tully et al. 1998). Undoing this correction means that an uncorrected inverse TF sample has a $V(M)$ slope steeper than the true slope. In the B band the effect is about 10–15% of the magnitude range of the sample (Tully et al. 1998), so the uncorrected inverse TF slope is $\sim 10 - 15\%$ higher. This could counteract the slope-shallowing effect described above. However, one must tread carefully when applying local extinction corrections to distant samples. Both the extinction effect and the inclination-induced offsets are reasons to attempt comparisons internal to the sample, spanning a range of redshifts.

The general effects of the lack of correction are small shifts in intercept and slope, and a substantial increase in scatter. If the TKRS galaxies with linewidths were all close to the thin rotating disk model, applying inclination and extinction corrections would greatly reduce the scatter in the Tully-Fisher relations fitted in Paper II. In fact, in Paper II we find that applying either the $\sin i$ inclination correction, or both inclination and extinction corrections, *does not* reduce the scatter in Tully-Fisher relations. A small amount of this can be due to statistical errors on inclination, but most is due to the diversity of kinematic properties, galaxies with non-disk shapes,

and motions that are not strictly rotation, as we show in Section 5.

4.4. Empirical dependence on slit position angle

Rotation curves of inclined disks should be harder to measure when the slit is not aligned close to the major axis. The modeling of NGC 7171 suggests that integrated velocity linewidths are not as severely affected by slit misalignments. The effect can be tested empirically for the TKRS sample since HST imaging allows measures of the galaxy position angles.

We used a compilation of measurements from ellipse fitting to the ACS i -band galaxy images, yielding ellipticity, position angle, and half-light radius. Segmentation images output by the SExtractor program (Bertin & Arnouts 1996) were used to mask out neighboring galaxies and the IRAF task `ellipse` was run to fit elliptical isophotes.¹⁰ Further results on the galaxy sizes will be reported separately (Melbourne et al. 2006). Here we use the ellipticities and position angles to determine slit misalignments.

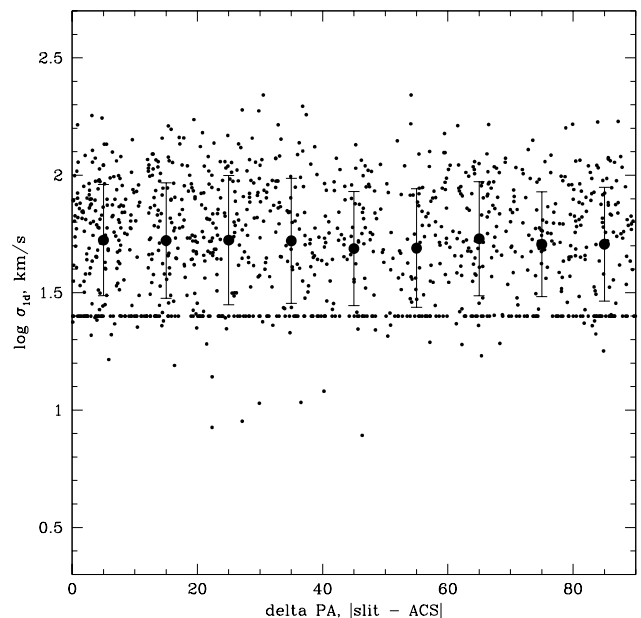


FIG. 12.— Integrated linewidth $\log \sigma_{1d}$ as a function of position angle misalignment: offset between slit PA and major axis PA from ellipse fits to HST/ACS images. Large points show the mean and RMS in bins of angle. The small points at $\log \sigma_{1d} = 1.4$ are the kinematically unresolved objects. There is no visible trend of measured 1-d linewidth with PA offset.

Figure 12 shows integrated linewidth $\log \sigma_{1d}$ as a function of the misalignment between slit and image position angle. The large points show the mean and RMS in bins of PA offset. (The slitmasks were designed based on PAs from ground based imaging before the HST catalog was available, so the slits are not exactly aligned with HST PAs.) Slit misalignment has no visible effect on linewidth

¹⁰ IRAF is distributed by NOAO, which is operated by AURA, Inc., under a cooperative agreement with the National Science Foundation.

measured from the 1-d spectrum. A fraction of the galaxies in this plot are nearly round, so that the PA is not very meaningful; removing these objects does not change the conclusion. A small trend with PA offset might be expected from the models in Figure 10, but galaxies that are not orderly rotating disks, and galaxies whose ellipticity and kinematics are misaligned, will weaken such a trend.

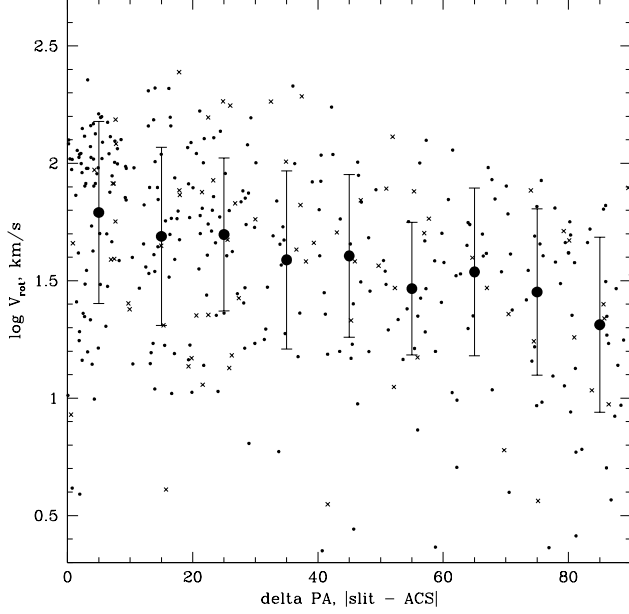


FIG. 13.— Rotation velocity $\log V_{rot}$ as a function of position angle misalignment, offset between slit PA and HST/ACS major axis PA. Round galaxies with ellipticity $e < 0.25$ are plotted as Xes, non-round galaxies are circles. Large points show the mean and RMS of non-round galaxies in bins of angle. Extracted rotation velocities are higher for aligned slits; there is a deficit of high V_{rot} for misaligned slits.

For the subsample of galaxies with 2-d rotation fits, Figure 13 shows the rotation velocity $\log V_{rot}$ as a function of the slit misalignment angle. Again, large points show the mean and RMS in bins of PA offset. Here, there is a strong effect: measured rotation velocity declines as misalignment increases, and there is a lack of high V_{rot} objects for misaligned slits, as expected. However, note that even aligned slits have a fair number of low V_{rot} objects.

Clearly, measuring rotation velocity from a misaligned slit is subject to large error, especially since ROTCURVE does not use a full 2-d model. For purposes of studying the properties of rotation velocity and dispersion in the next section, we split the sample into “aligned” and “misaligned” with $|\Delta PA| < 40^\circ$ and $> 40^\circ$. We also exclude the nearly-round galaxies with ellipticity $e < 0.25$ from the “aligned” subsample.

5. PROPERTIES OF SPATIALLY RESOLVED KINEMATICS

5.1. Rotation versus dispersion dominated galaxies

The two galaxies whose rotation and dispersion profiles are shown in Figure 3 exemplify a trend we found in the entire sample. In order to fit the kinematics, we had to

TABLE 3
CATALOG OF TKRS ROTATION AND DISPERSION FITS

TKRS ID	z^1	$ \Delta PA ^2$	V_{rot}^3	σ_{2d}^4	morphology ⁵
0000428	0.4870	13.2	14.0	15.0	hyphen
0000448	0.4724	70.1	80.0	40.1	—
0000555	0.4589	81.0	37.8	69.6	—
0000714	0.9434	52.8	21.6	48.8	—
0000760	0.5032	14.0	209.2	10.0	disk
0001126	0.9447	25.8	62.9	64.3	irregular
0001217	0.4587	0.8	4.1	59.4	merger
0001226	0.5023	13.7	0.0	65.0	irregular
0001289	0.1137	54.5	56.5	69.9	—
0001333	1.2960	80.1	46.9	74.4	—
0001432	0.7479	48.6	0.6	54.3	—
0001563	0.3758	16.4	157.0	5.0	edge-on
0001577	0.4855	2.1	110.2	5.0	disk
0001769	0.1192	66.3	50.0	65.1	—
0001808	0.0787	21.5	64.3	39.8	edge-on
0001861	1.3630	3.0	95.1	40.0	disk
0001923	0.2755	43.0	50.8	39.9	—
0001950	1.3640	45.3	21.4	89.5	—
0002011	0.4734	88.4	9.3	24.8	—
0002012	1.0010	0.4	104.4	55.0	disk

NOTE. — The complete version of this table is in the electronic edition of the Journal. The printed edition contains only a sample.

¹Redshift.

²Absolute value of the offset between DEIMOS slit position angle and photometric major axis PA in HST/ACS *I* images, degrees.

³Line-of-sight rotation velocity from seeing-compensated modeling of the 2-d spectra, km s^{-1} . For $|\Delta PA| \gtrsim 40^\circ$, rotation velocities are strongly affected by slit misalignment.

⁴Line-of-sight dispersion from seeing-compensated modeling of the 2-d spectra, km s^{-1} . Values are near-quantized in units of 5 km s^{-1} due to the model grid.

⁵Morphological type from visual classification. Only galaxies with $|\Delta PA| < 40$ and ellipticity > 0.25 were classified.

include both velocity V_{rot} and dispersion σ_{2d} in the 2-d modeling of ROTCURVE, discussed in Section 2.3. Quite a few galaxies like TKRS 5627 and 10023 show a low rotation velocity but a significant dispersion.

Table 3 lists galaxy ID, redshift, slit PA offset, and the fitted line-of-sight rotation and dispersion for the 380 galaxies with good ROTCURVE fits. It also includes morphological classifications for a subset of the galaxies, discussed further in Section 6. Because there are galaxies which appear not to be consistent with inclined thin rotating disks, we report the line-of-sight velocities rather than applying an ellipticity-based inclination correction. If a significant number of high-redshift galaxies are not circular rotating disks, the chain of reasoning from axis ratio to inclination to $\sin i$ correction breaks down.

The simulated seeing-blurred velocity fields in Section 4.2 suggest that observing a rotating galaxy with the slit along the minor axis yields a low velocity gradient but a central peak in velocity dispersion. These are found in our sample, but TKRS 5627 and 10023, shown in Figures 1, 2, and 3, are different. They exemplify a class of galaxies which have low rotation, high dispersion, and aligned slits ($|\Delta PA| < 40^\circ$), so that the lack of rotation is not due to slit misalignment. These galaxies also frequently show dispersion profiles which are not sharply peaked, although the limited spectral resolution of TKRS makes dispersion profiles rather noisy.

We classified galaxies into rotation- and dispersion-dominated, based on whether $V_{rot} > \sigma_{2d}$ or vice versa.

Figure 14 plots σ_{2d} versus V_{rot} ; the placement of the dividing line is somewhat arbitrary, but intended to separate galaxies whose main kinematic support is from orderly rotation, and galaxies where dispersion (or the disordered gas motions that σ_{2d} may represent) plays a major role. When roundish galaxies with $e < 0.25$ and those with misaligned slits, $|\Delta PA| > 40^\circ$, are excluded, there are 185 galaxies with good 2-d fits from ROTCURVE. Of these, 118 are rotation dominated and 67 (36%) are dispersion dominated. Thus two-thirds of the subsample have kinematics basically similar to local rotating galaxies – which was by no means guaranteed – but over one-third of this subsample have kinematics that are inconsistent with a thin rotating disk model.

The nature of the dispersion dominated galaxies is a puzzle. They are not literally dispersion-supported elliptical galaxies. Comparing rotation and dispersion dominated galaxies (RDGs and DDGs) in magnitude and color, the DDGs are only slightly different, 0.05 bluer in median $U - B$ and equal in median brightness, and their morphologies are late type; we discuss DDG and RDG properties further in Section 6. The DDGs’ velocity dispersion is unlikely to indicate a literal dynamically hot pressure-supported tracer population like stars in spheroidals. We are measuring velocities from nebular lines that come from $\sim 10^4$ K gas, so the dispersion in individual H II regions is only 8-10 km s $^{-1}$. The larger values of σ_{2d} found in DDGs could come from the relative motions of the ensemble of gas clouds – chaotic, disordered, or out-of-plane velocity fields that are smoothed over by the seeing, or that have strong misalignments between photometry and kinematics. However, the geometry of the motions and whether they will eventually dissipate and settle into a disk cannot be resolved in these spectra.

If the seeing blur caused a bias against the detection of rotation in small objects, it could make objects appear dispersion dominated by masking the true rotation gradient. In principle, the ROTCURVE fitting method is seeing-compensated. For a very small object with a rotation gradient that suffers greatly from seeing blur, it yields a shallow minimum in χ^2 ; models with an intrinsic rotation gradient and with a dispersion both fit the data, so there is a large error on V_{rot} rather than a bias. In practice, we rejected objects with a very small diameter of velocity data, $\lesssim 1''$. In Section 6 we discuss the sizes of RDGs and DDGs and show that the DDGs are only mildly smaller, so they are not simply caused by an observational bias against rotation. Intrinsic non-roundness or errors in the ellipticity and PA measurements could cause a few face-on disks to appear in the DDG sample, but there are too many elongated DDGs to explain away.

Dispersion dominated galaxies occur over the full redshift range of our sample and are not strictly a high-redshift population. Figure 15 plots magnitude against redshift for the sample with 2-d ROTCURVE modeling, with points coded for rotation or dispersion domination. DDGs exist at low redshift, but are relatively faint there; it is possible that the dispersion/rotation fraction is higher at high redshift, although the sample size and selection effects make any conclusion preliminary.

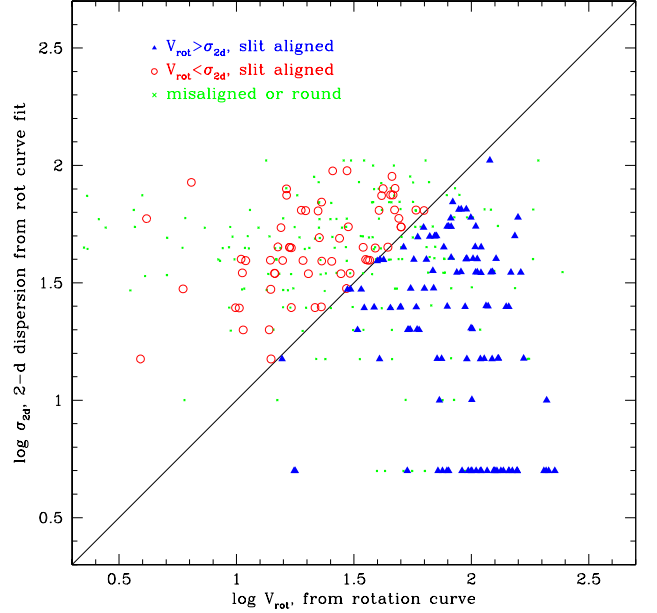


FIG. 14.— 2-d dispersion versus rotation velocity for galaxies with 2-d ROTCURVE modeling. Open circles: dispersion dominated galaxies, $V_{rot} < \sigma_{2d}$, with $e > 0.25$. Filled triangles: rotation dominated galaxies, $V_{rot} > \sigma_{2d}$, with $e > 0.25$. Small Xes: round galaxies or misaligned slits. We divide the galaxies into rotation and dispersion dominated at $V_{rot} = \sigma_{2d}$. The values of σ_{2d} are quantized in steps of 5 km s $^{-1}$ by the fitting method.

5.2. Comparison of integrated linewidths and spatially resolved kinematics

A key question for using linewidths of integrated emission as a characteristic velocity scale is how well they correlate with spatially resolved kinematic measures. In Section 4.2 we tested models of seeing-blurred integrated emission from a rotating disk and found that linewidth σ_{1d} correlated well with projected circular velocity $V_c \sin i$; the chief scatter between σ_{1d} and true V_c is induced by inclination. In this section we test the relation of linewidth to rotation and dispersion from spatially resolved fits empirically using the 1-d and 2-d kinematic fits in TKRS. These quantities are line-of-sight, so no inclination correction is applied.

The existence of rotation and dispersion dominated galaxies suggests that neither 2-d measure, V_{rot} nor σ_{2d} , by itself adequately represents the velocity scale of every distant galaxy. Figures 16 and 17 plot the 2-d velocity and dispersion, V_{rot} and σ_{2d} , against the 1-d integrated linewidth, σ_{1d} . Point types are coded by whether the galaxy’s 2-d kinematics are rotation or dispersion dominated. The clustering of points with $\log \sigma_{1d} = 1.4$ are galaxies kinematically unresolved in 1-d.

Figures 16 and 17 are the flip-side of each other. Each 2-d quantity, when it dominates, correlates with the 1-d measure σ_{1d} , but falls well below σ_{1d} when it does not dominate. Either used alone would leave some galaxies with egregiously small velocities.

For rotation dominated galaxies, there is a fair amount of scatter between V_{rot} and σ_{1d} , but in general these

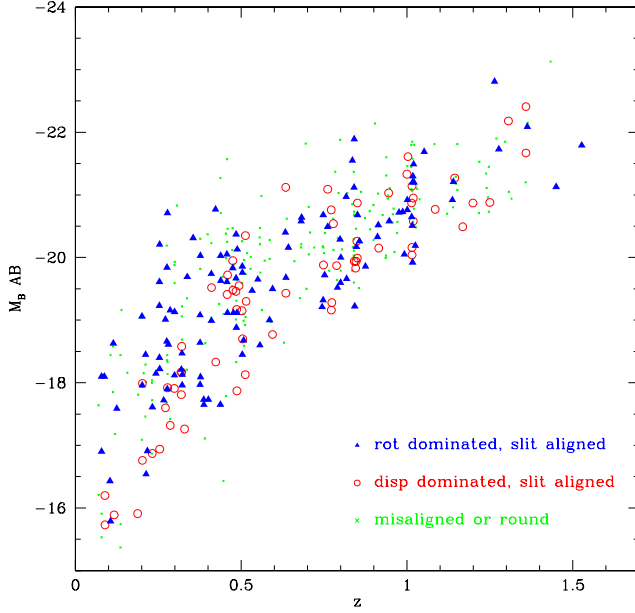


FIG. 15.— Magnitude versus redshift for galaxies with 2-d ROTCURVE modeling. Open circles: dispersion dominated galaxies, $V_{rot} < \sigma_{2d}$, with $e > 0.25$. Filled triangles: rotation dominated galaxies, $V_{rot} > \sigma_{2d}$, with $e > 0.25$. Small Xes: round galaxies or misaligned slits. Dispersion dominated galaxies exist at low redshift, but are relatively faint. There is not strong evidence for redshift evolution in the rotation/dispersion fraction, but possibly bright dispersion dominated galaxies are only found at high redshift.

quantities are correlated, with σ_{1d} offset below V_{rot} . But for dispersion dominated galaxies, V_{rot} is low and does not reflect the kinematic support seen in σ_{1d} . Conversely, σ_{2d} correlates well with σ_{1d} in dispersion dominated galaxies. But rotation dominated galaxies can be fit without requiring 2-d dispersion, so σ_{2d} falls below σ_{1d} . In the RDGs, σ_{1d} is capturing the seeing-induced dispersion.

The inadequacy of each 2-d quantity V_{rot} and σ_{2d} by itself motivated the design of ROTCURVE, which fits both simultaneously. To represent a characteristic velocity derived from the 2-d ROTCURVE fits, we define a “combined velocity scale” S_K :

$$S_K^2 = KV_{rot}^2 + \sigma_{2d}^2, \quad (5)$$

where K is a constant ≤ 1 . The scale S_K combines rotation and pressure or random/disordered-motion support, just as Tully-Fisher studies have done to model an observed integrated H I linewidth (e.g. Tully & Fouque 1985). The simplest combination is $S_{1.0}$, with $K = 1$. This is in some sense an estimator of rotation velocity plus a turbulent-motion correction.

However, setting $K < 1$ makes S_K a better estimator of the velocity dispersion σ of the entire potential, because rotation velocity and dispersion contribute differently to the support of a gravitationally bound system. For example, in an isothermal potential with a flat rotation curve, a population with isotropic velocity dispersion and no net rotation has $\sigma = V_c/\sqrt{2}$, suggesting

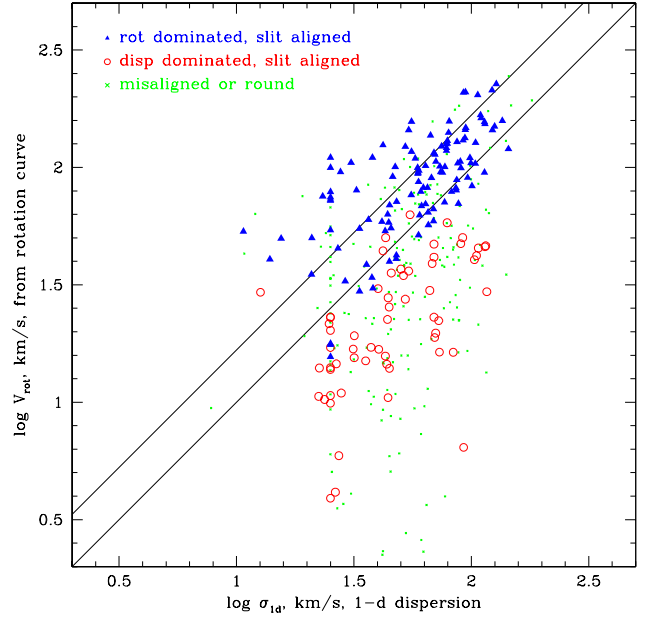


FIG. 16.— Rotation velocity from the 2-d ROTCURVE modeling, $\log V_{rot}$, versus integrated linewidth $\log \sigma_{1d}$. Open circles: dispersion dominated galaxies, $V_{rot} < \sigma_{2d}$, with $e > 0.25$. Filled triangles: rotation dominated galaxies, $V_{rot} > \sigma_{2d}$, with $e > 0.25$. Small Xes: round galaxies or misaligned slits. The galaxies at $\log \sigma_{1d} = 1.4$ are kinematically unresolved in the 1-d linewidth. The diagonal lines are the 1:1 line and the Rix et al. (1997) $\sigma = 0.6V_c$ line. For dispersion dominated galaxies, σ_{1d} captures the velocity scale but V_{rot} goes to small values.

that with $K = 0.5$, $S_{0.5}$ is a good estimator of σ of the potential. In general, for a spherically symmetric tracer distribution with density $\propto r^{-\alpha}$ and isotropic velocity dispersion, if V_c varies slowly with radius, $\sigma = V_c/\sqrt{\alpha}$ (Binney & Tremaine 1987). Real galaxies in the range at or beyond the peak of the baryonic contribution to the rotation curve, where rotation curves are measured, have $\alpha = 2 - 3$ for a spherized mass distribution, so $K = 0.3 - 0.5$ is reasonable.

Figures 18 and 19 plot the combined velocity scales $S_{1.0}$ and $S_{0.5}$ against 1-d linewidth σ_{1d} . Combined velocity alleviates the shortcomings of V_{rot} and σ_{2d} , eliminating artificially low velocity measurements. Both $S_{1.0}$ and $S_{0.5}$ show strong correlations with σ_{1d} . For the subsample with aligned slits and $e > 0.25$, the mean offset $\log S_{1.0} - \log \sigma_{1d}$ is 0.15 dex with RMS 0.17 dex; for $S_{0.5}$ the mean and RMS log offset are 0.06 and 0.14. The rotation estimator $S_{1.0}$ shows its rotation velocity heritage; rotation dominated galaxies have $S_{1.0} > \sigma_{1d}$, relatively close to the $\sigma = 0.6V_c$ line of Rix et al. (1997). RDGs and DDGs are offset in $S_{1.0}$; the offset in $S_{0.5}$ is smaller. When the dispersion-analog $S_{0.5}$ is plotted against σ_{1d} , the correlation with σ_{1d} tightens, and the offset between $S_{0.5}$ and σ_{1d} is reduced, because both are estimating a velocity dispersion of the potential.

The good correlation between 1-d integrated linewidth and the combined velocity scale from 2-d rotation and dispersion fits has two major implications. First, 1-d linewidth is a reliable representation of the more sophisti-

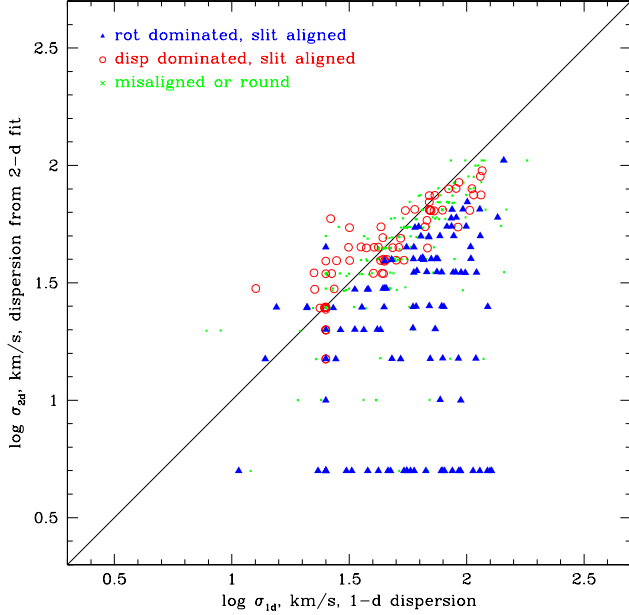


FIG. 17.— Dispersion from the 2-d ROTCURVE modeling, $\log \sigma_{2d}$, versus integrated linewidth $\log \sigma_{1d}$. The σ_{2d} values are quantized by fitting on a 5 km s^{-1} model grid. Open circles: dispersion dominated galaxies, $V_{rot} < \sigma_{2d}$, with $e > 0.25$. Filled triangles: rotation dominated galaxies, $V_{rot} > \sigma_{2d}$, with $e > 0.25$. Small Xes: round galaxies or misaligned slits. The diagonal line is the 1:1 line. For dispersion dominated galaxies, σ_{1d} and σ_{2d} are correlated; for rotation dominated galaxies, σ_{1d} captures the velocity scale while σ_{2d} becomes small.

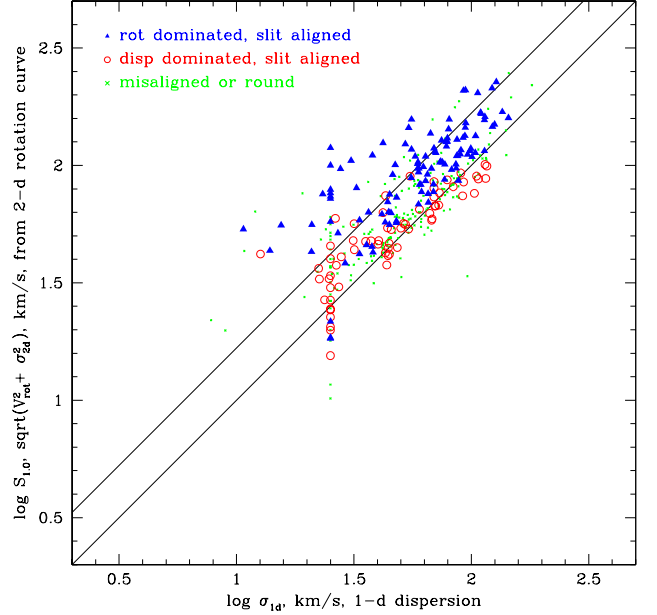


FIG. 18.— Combined velocity, $S_{1.0}^2 = V_{rot}^2 + \sigma_{2d}^2$: $\log S_{1.0}$ versus integrated linewidth $\log \sigma_{1d}$. Open circles: dispersion dominated galaxies, $V_{rot} < \sigma_{2d}$, with $e > 0.25$. Filled triangles: rotation dominated galaxies, $V_{rot} > \sigma_{2d}$, with $e > 0.25$. Small Xes: round galaxies and those with large error on V_{rot} and σ_{2d} . The diagonal lines are the 1:1 line and the Rix et al. (1997) $\sigma = 0.6V_c$ line. Linewidth and $S_{1.0}$ are correlated, falling closer to the 1:1 line for dispersion dominated and to the Rix et al. line for rotation dominated galaxies.

cated 2-d kinematics. As suggested by the simulations in Section 4.2, the seeing is a powerful integrator. The 1-d linewidth can be used as a kinematic measure when estimating dynamical masses, although the $\sigma_{1d} \sim 0.6V_c$ and the substantial scatter should be kept in mind. Second, 2-d rotation velocity alone does not completely account for the kinematic support for all galaxies. For galaxies that are selected to have visibly rotation-dominated kinematics, V_{rot} is adequate, but for broader samples, V_{rot} alone will not suffice. Constructing a Tully-Fisher relation using V_{rot} only will push galaxies with $\sigma_{2d} > V_{rot}$ to erroneously low velocity, as seen in Figure 16.

6. DISCUSSION: THE NATURE OF ROTATION AND DISPERSION DOMINATED GALAXIES

The existence of rotation and dispersion dominated emission line galaxies – essentially two modes of dynamical support, or a sort of kinematic morphology – raises the question of their nature and evolution. Rotation is well understood in local galaxies; dispersion dominated galaxies are the real puzzle. The size of the TKRS sample yields enough RDGs and DDGs to compare the physical properties and morphologies of these galaxies.

Several other studies of intermediate and high redshift galaxies have found objects inconsistent with rotation, similar to the DDGs. Simard & Pritchett (1998) found 25% of their galaxies had “kinematically anomalous” [O II] emission. These objects had centrally concentrated emission; we find below that DDGs are smaller in both continuum and emission. Erb et al. (2004) found that

spectra of 13 elongated galaxies at $z \sim 2$ rarely show rotation. Bershadsky et al. (2005) obtained HST/STIS spectra of six luminous compact blue galaxies and found low V/σ ; the STIS velocity dispersion confirmed ground-based integrated linewidth. From integral field spectroscopy, Flores et al. (2006) found that $\sim 2/3$ of 35 galaxies at $0.4 < z < 0.75$ had either mildly decentered or non-rotating kinematics; some of these may be dispersion dominated. Our TKRS survey establishes that the dispersion dominated galaxies are relatively common and not restricted to specially selected samples.

It is unclear what the local counterparts of dispersion dominated galaxies could be. Many local studies of galaxy kinematics, in order to study the distance scale or rotation curves and dark matter, have selected against galaxies with disordered kinematics. However, even very small galaxies down to $M_B \sim -15 - 16$ are generally dominated by rotation (e.g. Swaters et al. 2002). Tully-Fisher studies have considered the contribution of turbulent motions to the linewidth; Tully & Fouque (1985) claim that turbulent motions are only significant for very small rotation velocities $V \lesssim 25 \text{ km s}^{-1}$, but this is based on an idealized model. Kannappan & Barton (2004) find a larger percentage of kinematically anomalous galaxies in close pairs; these mostly show distorted or truncated rotation curves, but a few are unusual enough that seeing-blur could make rotation gradients undetectable. It is also possible that evolution makes bright dispersion dominated emission line galaxies rare at the present day.

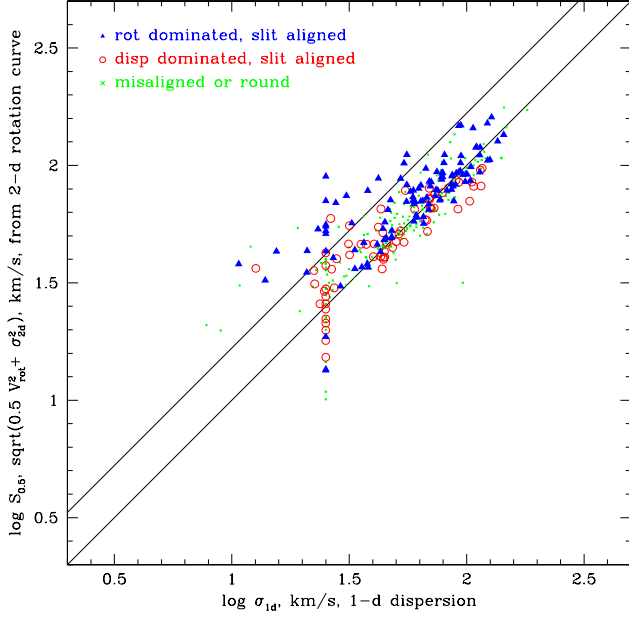


FIG. 19.— Combined velocity, $S_{0.5}^2 = 0.5V_{rot}^2 + \sigma_{2d}^2$: $\log S_{0.5}$ versus integrated linewidth $\log \sigma_{1d}$. Open circles: dispersion dominated galaxies, $V_{rot} < \sigma_{2d}$, with $e > 0.25$. Filled triangles: rotation dominated galaxies, $V_{rot} > \sigma_{2d}$, with $e > 0.25$. Small Xes: round galaxies and those with large error on V_{rot} and σ_{2d} . The diagonal lines are the 1:1 line and the Rix et al. (1997) $\sigma = 0.6V_c$ line. Linewidth and $S_{0.5}$ are correlated; the 0.5 prefactor makes the combined velocity width a better estimate of velocity dispersion, so that the correlation is tighter and the galaxies closer to the 1:1 line.

6.1. Comparative Properties of Rotation and Dispersion Dominated Galaxies

Rotation and dispersion dominated galaxies do exist over the full redshift range of our sample, as seen in Figure 15. There is some sign that at $z \lesssim 0.4$, DDGs are only found at faint magnitudes. This might reflect an evolution either in kinematics or in magnitude and emission strength. To compare the properties of luminous RDGs and DDGs, and to avoid being pulled by faint objects visible only at low redshift, we show distributions of galaxy properties for a sample restricted to $z > 0.4$, and with aligned slits and ellipticity $e > 0.25$ as before.

The distributions of $z > 0.4$ RDG and DDG restframe magnitude and color M_B and $U - B$ are shown in Figures 20 and 21. At $z > 0.4$, the two types have indistinguishable magnitude distributions. The DDGs are bluer in the median than the RDGs, but only by 0.05 mag. Comparing the RDG and DDG distributions with the Kolmogorov-Smirnov statistic gives a 93% probability that they are identical in M_B and a 15% probability that they are identical in $U - B$. The DDG color distribution covers almost the whole of the range of the blue galaxy population, so it appears that DDGs are not solely unusual blue objects, e.g. compact H II regions or extreme starbursts.

The size distributions of $z > 0.4$ RDGs and DDGs are shown in continuum and in emission, in Figures 22 and 23. Figure 22 plots the physical half-light radius R_{hl} in

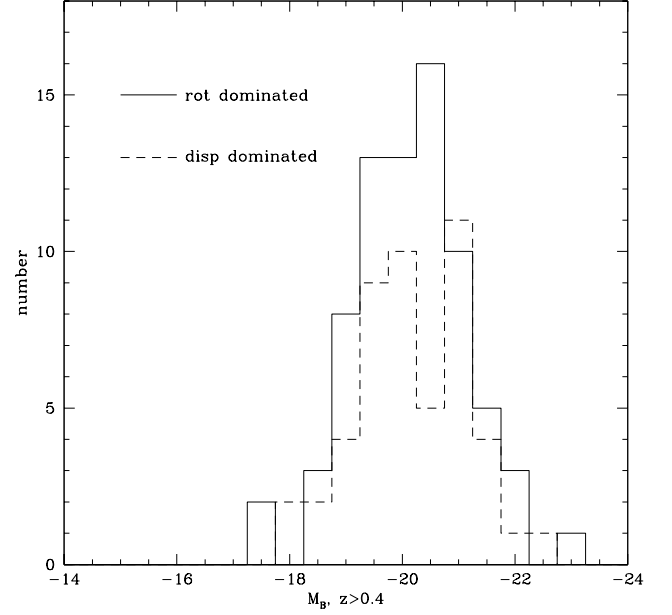


FIG. 20.— Magnitude distribution in restframe M_B of rotation and dispersion dominated galaxies at $z > 0.4$, with aligned slits and $e > 0.25$. Solid line: rotation dominated galaxies, $V_{rot} > \sigma_{2d}$. Dashed line: dispersion dominated galaxies, $V_{rot} < \sigma_{2d}$. At high redshift, RDGs and DDGs are equally bright.

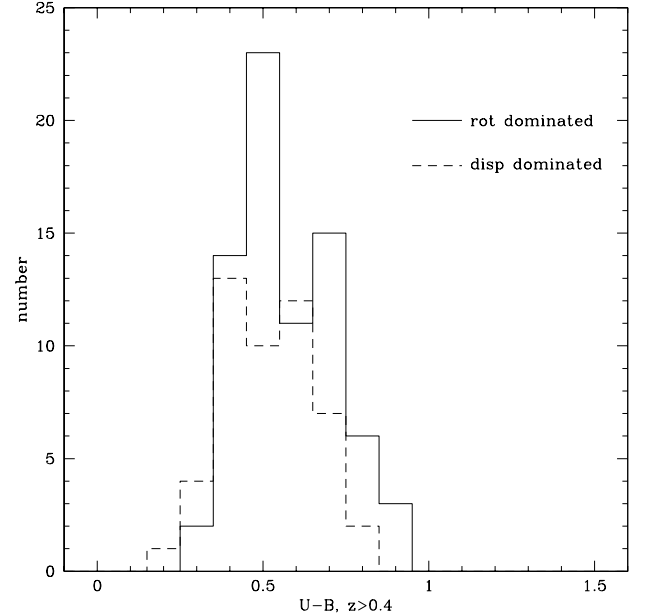


FIG. 21.— Color distribution in restframe $U - B$ of rotation and dispersion dominated galaxies at $z > 0.4$, with aligned slits and $e > 0.25$. Solid line: rotation dominated galaxies, $V_{rot} > \sigma_{2d}$. Dashed line: dispersion dominated galaxies, $V_{rot} < \sigma_{2d}$. RDGs are slightly redder than DDGs.

kpc from the HST ACS I images, while Figure 23 plots the observed emission diameter in arcsec, D_{em} , using

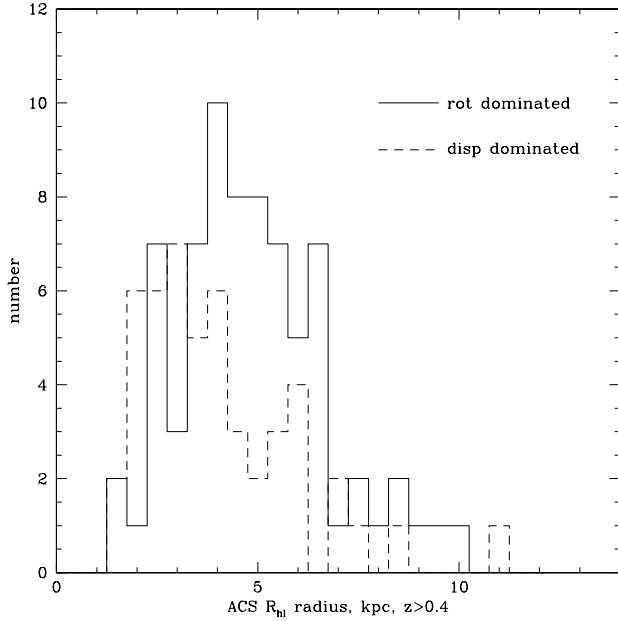


FIG. 22.— Radius distribution in half-light radius R_{hl} , kpc, from HST images, for rotation and dispersion dominated galaxies at $z > 0.4$, with aligned slits and $e > 0.25$. Solid line: rotation dominated galaxies, $V_{rot} > \sigma_{2d}$. Dashed line: dispersion dominated galaxies, $V_{rot} < \sigma_{2d}$. RDGs are larger in the mean than DDGs, though the size distributions overlap.

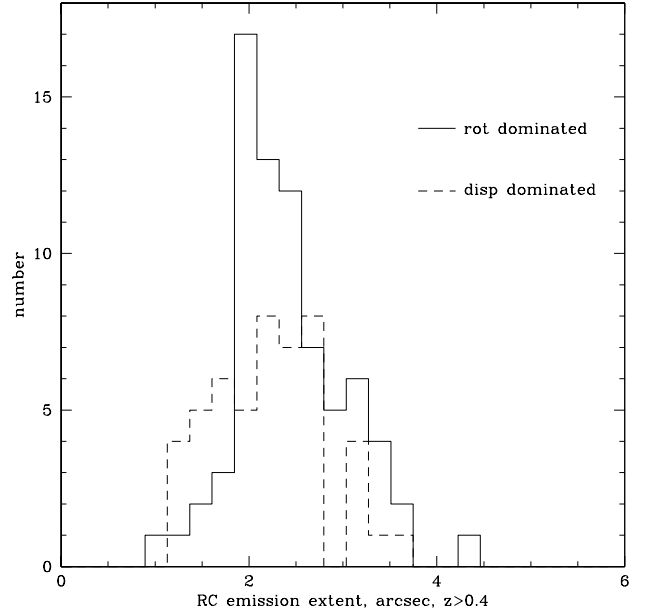


FIG. 23.— Emission extent: the total range (diameter), in arcsec, of data used in the rotation/dispersion fit in the Keck spectra, for rotation and dispersion dominated galaxies at $z > 0.4$, with aligned slits and $e > 0.25$. Solid line: rotation dominated galaxies, $V_{rot} > \sigma_{2d}$. Dashed line: dispersion dominated galaxies, $V_{rot} < \sigma_{2d}$. RDGs are larger in the mean than DDGs, though less so than in half-light radius. The ranges in emission extent are similar, implying that DDGs are real and not just objects too small to detect rotation in ground-based spectra.

the range of data in the Keck spectra deemed good by ROTCURVE fitting.

Here there is a difference between DDGs and RDGs. Dispersion dominated galaxies are smaller in both size measures. The offset is more noticeable in the physical radius R_{hl} . Although the range of sizes for DDGs is about as broad as for RDGs, the DDGs are somewhat smaller in the average: the medians of R_{hl} are 3.7 and 4.7 kpc for DDGs and RDGs. The DDGs are similar in luminosity to RDGs but smaller in radius, so they are somewhat more compact.

The emission diameter D_{em} plotted in 23 is the angular extent from the first to last row (inclusive) in the Keck spectrum of the data that ROTCURVE deemed good for fitting. There is a mild offset, with rotation dominated galaxies being larger in the average, but the RDGs and DDGs span the same range of angular sizes. The medians of D_{em} are 2.26" and 2.38" for DDGs and RDGs. The distribution of D_{em} is limited at the small end because the rotation curve sample was selected by enforcing a lower limit in ground-based angular size of $\text{FWHM} = 0.94''$. The K-S statistic gives a 2% probability that the RDG and DDG distributions are identical in R_{hl} and a 12% probability that they are identical in D_{em} . From the K-S tests, the only firm difference between RDG and DDG properties is in the physical radius R_{hl} . The two types of galaxy are not as different in D_{em} as they are in HST-measured physical radius; this could be caused by the selection on ground-based size; by seeing blur; by differences in the falloff of the light profiles; and/or by threshold effects, since D_{em} measures where the emission strength drops below some value that yields

a reliable velocity.

The chief point of Figure 23 is that the DDGs and RDGs in our rotation curve sample span a similar range of angular extent as measured on the 2-d spectra. This implies that the dispersion dominated galaxies are genuinely non-rotating in their mean emission. It argues against the possibility that DDGs are simply an observational bias in small galaxies, caused by emission which does not extend far enough to detect rotation, alluded to in Section 5.1. However, such a bias might re-appear in samples without an angular size lower limit.

6.2. Morphologies of Rotation and Dispersion Dominated Galaxies

To explore further any systematic differences between rotation and dispersion dominated galaxies, we made a morphological classification of the sample of 116 RDGs and 67 DDGs that have aligned slits and ellipticity > 0.25 . We inspected ACS *I*-band images from the GOODS-N data. The classifications are cataloged in Table 3.

Because the physical resolution is limited and high redshift galaxies are known to exhibit a greater degree of morphological peculiarity (e.g. Abraham et al. 1996), we defined a simplified system of morphological types. We found no spheroidals in the RDG/DDG sample. The classes are: disks, Sb-Sd; irregulars, both low and high surface brightness; edge-on disks; “chain” and “hyphen” galaxies; and mergers. Chain galaxies are elongated ob-

TABLE 4
MORPHOLOGIES OF ROTATION AND DISPERSION
DOMINATED GALAXIES

Type	RDG all z	RDG $z > 0.4$	DDG all z	DDG $z > 0.4$
spheroidal	0%	0%	0%	0%
disk	42%	45%	22%	27%
edge-on disk	16%	8%	2%	0%
irregular	31%	32%	43%	41%
chain/hyphen	7%	10%	25%	22%
merger	3%	5%	8%	10%
total	116	74	67	49

jects with bright knots (e.g. Cowie, Hu, & Songaila 1995). Hyphen galaxies are thin, small but elongated, with little substructure. We only defined galaxies as mergers if they clearly had multiple components, tidal tails, or major disturbances associated with mergers. Many high- z galaxies are somewhat peculiar or asymmetric and we did not count these as evidence of mergers. The percentages of morphological types for RDGs and DDGs are listed in Table 4, for both the full sample and the sample restricted to $z > 0.4$, where RDGs and DDGs have similar luminosity.

The clearest results from Table 4 are that rotation dominated galaxies are generally disk, or irregular, and very rarely chain or hyphen galaxies. Dispersion dominated galaxies sometimes appear disk, but are more often irregular, and a substantial number are chain or hyphen galaxies. Hardly any DDGs were edge-on disks, which is understandable since these are most likely to have detectable rotation. Mergers are not a large fraction of either RDGs or DDGs.

Restricting the sample to $z > 0.4$ changes the ratios little, other than to decrease the number of edge-on disk RDGs. There is a definite offset in morphology between RDGs and DDGs, but also substantial overlap. These morphologies are subjective; the link between kinematic and photometric morphologies will be addressed further with larger samples and objective measures in the DEEP2 survey.

A significant number of galaxies were classed as chain or hyphen, types which are rare at low redshift. Two-thirds of the chain/hyphen galaxies were DDGs; only one-third of these elongated objects were dominated by rotation. TKRS 5627 shown in Figures 1 and 3 is an example of a chain galaxy, elongated but nonrotating. Similar objects have been found at $z \sim 2$ by Erb et al. (2004): their slit spectra of 13 elongated galaxies showed dispersion, but rarely rotation. These results suggest that kinematic surveys must use caution in interpreting ellipticity: elongated objects may not be inclined disks and may not be rotating.

The higher fraction of peculiar objects at high redshift suggests that galaxies evolve in photometric morphology, with a greater fraction of seemingly irregular galaxies at $z \sim 1$ (e.g. Abraham et al. 1996; Lotz et al. 2006). Possibly they also evolve in kinematic morphology. Luminous dispersion dominated galaxies appear at $z \sim 1$ but are uncommon locally; even faint local blue galaxies are usually dominated by rotation (e.g. Swaters et

al. 2002). Perhaps DDGs settle from a disordered or non-planar kinematic state into more orderly rotation; or their disordered kinematics are dominated by bright star forming regions which then fade to allow a more ordered background to be seen; or they evolve in luminosity by fading more than the overall population; or they cease forming stars and both fade and drop out of emission-line kinematic samples, leaving behind dispersion-supported faint red galaxies.

7. CONCLUSIONS

We have measured line-of-sight kinematic linewidths σ_{1d} for ~ 1000 galaxies in the Team Keck survey of the GOODS-N field and spatially resolved line-of-sight rotation (V_{rot}) and dispersion (σ_{2d}) profiles for 380 of these. Most galaxies with linewidths are on the blue side of the color bimodality. Linewidths from integrated spectra are a measure of internal kinematics that is relatively robust against observational effects, based on simulations of velocity fields and on comparisons of the linewidths with the spatially resolved kinematics. However, the unknown geometries of high-redshift velocity fields, scatter in galaxy ellipticities, and the lack of correction for projection into radial velocities mean that there is a fair amount of scatter between an individual galaxy linewidth measurement and a true circular velocity or dynamical mass estimate. For rotating galaxies, $\sigma_{1d} \sim 0.6V_c$ in the mean, due to a combination of the inclination and the fact that σ_{1d} is less than line-of-sight V_{rot} ; this factor should be kept in mind when estimating dynamical masses.

The rotation and dispersion profiles of spatially resolved galaxies show that not all galaxies exhibit a conventional rotation curve. Galaxies can be roughly divided into rotation and dispersion dominated, with $V_{rot} > \sigma_{2d}$ or vice versa. Dispersion dominated galaxies are blue, mostly irregular, and are not ellipticals; they probably have an effective dispersion, from disordered kinematics which are integrated over by the seeing. Dispersion dominated galaxies exist at all redshifts in our sample, but low- z DDGs are quite faint.

When line-of-sight rotation and dispersion are combined to make an estimate of the overall dispersion of the potential, as in $S_{0.5}^2 = 0.5V_{rot}^2 + \sigma_{2d}^2$, the result correlates well with the integrated linewidth σ_{1d} , demonstrating both that σ_{1d} is a robust velocity indicator and that it is possible to construct scaling relations with velocity for a population of diverse kinematic properties. In Paper II we use the linewidths to measure evolution in the Tully-Fisher relation.

At $z \sim 1$, rotation and dispersion dominated galaxies have similar magnitudes and colors, but somewhat different size and morphology distributions. Rotation dominated galaxies are mostly disk and irregular types; dispersion dominated galaxies are in the mean smaller in physical half-light radius, and $\sim 60\%$ of DDGs are irregular and chain/hyphen types. Only a small fraction of either RDGs or DDGs are obvious mergers. About two-thirds of chain and hyphen galaxies are dispersion dominated: elongated high-redshift objects cannot be assumed to be inclined rotating disks. It is not clear what the local counterparts of dispersion dominated galaxies might be; integral field spectroscopy, especially with adaptive optics, may shed some light on their nature at

high redshift.

There is some evidence that dispersion dominated galaxies are rare at bright magnitudes at low redshift, just as previous studies have shown that irregular photometric morphologies in bright galaxies are more common at high redshift than locally (e.g. Abraham et al. 1996; Lotz et al. 2006). It is possible that galaxies evolve in kinematic morphology, settling into ordered rotation, or that luminosity evolution causes them to appear more ordered, or to drop out of bright emission-line samples. These and other possibilities are avenues for further study with larger samples and quantitative morphological measurements.

We dedicate this paper to the memory of Bob Schommer.

REFERENCES

- Abraham, R.G., van den Bergh, S., Glazebrook, K., Ellis, R.S., Santiago, B.X., Surma, P., & Griffiths, R.E. 1996, *ApJS*, 107, 1
- Bamford, S.P., Milvang-Jensen, B., Aragón-Salamanca, A., & Simard, L. 2005, *MNRAS*, 361, 109
- Bamford, S.P., Aragón-Salamanca, A., & Milvang-Jensen, B. 2006, *MNRAS*, 366, 308
- Barton, E.J., Geller, M.J., Bromley, B.C., van Zee, L., & Kenyon, S.J. 2001, *AJ*, 121, 625
- Barton, E.J., & van Zee, L. 2001, *ApJ*, 550, L35
- Bell, E. F., Wolf, C., Meisenheimer, K., Rix, H.-W., Borch, A., Dye, S., Kleinheinrich, M., & McIntosh, D. H. 2004, *ApJ*, 608, 752
- Bershady, M.A., Vils, M., Hoyos, C., Guzman, R., & Koo, D.C. 2005, in *ASSL Vol. 329: Starbursts: From 30 Doradus to Lyman Break Galaxies*, 177
- Bertin, E., & Arnouts, S. 1996, *A&AS*, 117, 393
- Binney, J., & Tremaine, S. 1987, *Galactic Dynamics*, (Princeton: Princeton U.P.)
- Böhm, A., et al. 2004, *A&A*, 420, 97
- Capak, P., et al. 2004, *AJ*, 127, 180
- Conselice, C.J., Bundy, K., Ellis, R.S., Brichmann, J., Vogt, N.P., & Phillips, A.C. 2005, *ApJ*, 628, 160
- Cowie, L.L., Hu, E.M., & Songaila, A. 1995, *AJ*, 110, 1576
- Davis, M. et al. 2003, *Proc. SPIE*, 4834, 161
- Erb, D.K., Steidel, C.C., Shapley, A.E., Pettini, M., & Adelberger, K.L. 2004, *ApJ*, 612, 122
- Fioc, M., & Rocca-Volmerange, B. 1997, *A&A*, 326, 950
- Flores, H., Hammer, F., Puech, M., Amram, P. & Balkowski, C. 2006, *A&A*, in press, astro-ph/0603563
- Gialalisco, M., et al. 2004, *ApJ*, 600, L93
- Giovanelli, R., Haynes, M.P., Salzer, J.J., Wegner, G., da Costa, L.N., & Freudling, W. 1995, *AJ*, 110, 1059
- Kannappan, S.J., & Barton, E.J. 2004, *AJ*, 127, 2694
- Kinney, A. L., Calzetti, D., Bohlin, R. C., McQuade, K., Storchi-Bergmann, T., & Schmitt, H. R. 1996, *ApJ*, 467, 38
- Kobulnicky, H.A., & Gebhardt, K. 2000, *AJ*, 119, 1608
- Koo, D.C., Guzman, R., Faber, S.M., Illingworth, G.D., Bershady, M.A., Kron, R.G., & Takamiya, M. 1995, *ApJ*, 440, L49
- Lehnert, M.D., & Heckman, T.M. 1996, *ApJ*, 472, 546
- Lotz, J.M. et al. 2006, *ApJ*, submitted, astro-ph/0602088
- Mallén-Ornelas, G., Lilly, S.J., Crampton, D., & Schade, D. 1999, *ApJ*, 518, L83
- Melbourne, J., et al. 2006, *ApJ*, submitted, astro-ph/0602088
- Metevier, A.J., Koo, D.C., Simard, L., & Phillips, A.C. 2006, *ApJ*, 643, 764
- Milvang-Jensen, B., Aragón-Salamanca, A., Hau, G.K.T., Jørgensen, I., & Hjorth, J. 2003, *MNRAS*, 339, L1
- Nakamura, O., Aragón-Salamanca, A., Milvang-Jensen, B., Arimoto, N., Ikuta, C., & Bamford, S.P. 2006, *MNRAS*, 366, 144
- Palunas, P. 1996, PhD thesis, Rutgers University
- Palunas, P., & Williams, T.B. 2000, *AJ*, 120, 2884
- Pisano, D.J., Kobulnicky, H.A., Guzman, R., Gallego, J., & Bershady, M.A. 2001, *AJ*, 122, 1194
- Press, W.H., Flannery, B.P., Teukolsky, S.A. & Vetterling, W.T. 1992, *Numerical Recipes*, (Cambridge: Cambridge U.P.)
- Rix, H., Guhathakurta, P., Colless, M., & Ing, K. 1997, *MNRAS*, 285, 779
- Sakai, S. et al. 2000, *ApJ*, 529, 698
- Simard, L., & Pritchett, C.J. 1998, *ApJ*, 505, 96
- Strateva, I., et al. 2001, *AJ*, 122, 1861
- Swaters, R.A., van Albada, T.S., van der Hulst, J.M., & Sancisi, R. 2002, *A&A*, 390, 829
- Tully, R.B. & Fouque, P. 1985, *ApJS*, 58, 67
- Tully, R.B., Pierce, M.J., Huang, J., Saunders, W., Verheijen, M.A.W., & Witchalls, P.L. 1998, *AJ*, 115, 2264
- Vogt, N.P., et al. 1996, *ApJ*, 465, L15
- Vogt, N.P., et al. 1997, *ApJ*, 479, L121
- Vogt, N.P. 2000, *ASP Conf. Ser.* 197: Dynamics of Galaxies: from the Early Universe to the Present, 197, 435
- Weiner, B.J., Williams, T.B., van Gorkom, J.H., & Sellwood, J.A. 2001, *ApJ*, 546, 916
- Weiner, B.J., et al. 2005, *ApJ*, 620, 595
- Weiner, B.J., et al. 2006, *ApJ*, (Paper II)
- Willmer, C.N.A., et al. 2006, *ApJ*, in press
- Wirth, G.D., et al. 2004, *AJ*, 127, 3121
- Ziegler, B.L., et al. 2002, *ApJ*, 564, L69